



1 **High-Resolution Data Assimilation for Two Maritime Extreme Weather**
2 **Events: A comparison between 3DVar and EnKF.**

3
4 Diego S. Carrió¹, Vincenzo Mazzarella², Rossella Ferretti²
5

6 ¹*Meteorology Group, Department of Physics, University of the Balearic Islands, Palma, Spain*

7 ²*CETEMPS, Department of Physical and Chemical Sciences, University of L'Aquila, L'aquila 67100,*
8 *Italy*

9

10 **Abstract**

11 *Populated coastal regions in the Mediterranean are known to be severely affected by extreme weather*
12 *events. Generally, they are initiated over maritime regions, where a lack of in-situ observations is*
13 *present, hampering the initial conditions estimations and hence, the forecast accuracy. To face this*
14 *problem, Data Assimilation (DA) is used to improve the estimation of the initial conditions and their*
15 *respective forecasts. Although comparisons between different DA methods have been performed at*
16 *global scales, few studies are performed at high-resolution, focusing on extreme weather events*
17 *triggered over the sea and enhanced by complex topographic regions. In this study, we investigate the*
18 *role of assimilating different types of conventional and remote-sensing observations using the*
19 *variational 3DVar and the ensemble-based EnKF, which are of the most common DA schemes used*
20 *globally at National Weather Centers. To this aim, two different events are chosen because of both the*
21 *different areas of occurrence and the triggering mechanisms. Both the 3DVar and the EnKF are used*
22 *at convection permitting scales to improve the predictability of these two high-impact coastal extreme*
23 *weather episodes, which were poorly predicted by numerical weather prediction models: (a) the heavy*
24 *precipitation event IOP13 and (b) the intense Mediterranean Tropical-like cyclone Qendresa. Results*
25 *show that the EnKF and 3DVar perform similarly for the IOP13 event for most of the verification*
26 *metrics, although looking at the ROC and AUC scores, the EnKF clearly outperforms the 3DVar.*
27 *However, the ensemble mean of the EnKF is in general worse than the 3DVar for Qendresa, although*
28 *some of the ensemble members of the EnKF individually outperforms the 3DVar allowing for gaining*
29 *information on the physics of the event and hence the benefits of using an ensemble-based DA scheme.*

30

31 *Correspondence: Diego S. Carrió, University of the Balearic Islands, 07122, Cra. Valldemossa km 7.5,*
32 *Balearic Islands, Palma (Spain)*

33

34 *Email: diego.carrio@uib.es*

35

36 *Keywords: Variational Data Assimilation (3DVar), ensemble data assimilation (EnKF), low-predictable*
37 *weather events, extreme weather events, high-resolution numerical forecasts.*

38

39

40

41

42

43

44

45



46 1. Introduction

47 The Mediterranean basin is recognized as one of the geographical regions most frequently
48 affected by high impact weather events in the world (Petterssen, 1956). The Mediterranean
49 region has a natural disposition for these events because of its singular orographic features,
50 which include having a relatively warm sea surrounded by complex terrain. This geographical
51 configuration forces the warm and moist airflow to lift, favoring condensation and triggering
52 convection. Hazardous weather events in this region, such as heavy precipitation (e.g., flash
53 floods, snowstorms), cyclogenesis or windstorms (e.g., squall lines, tornadic thunderstorms),
54 produce huge economic, injury and human losses in populated coastal regions (e.g., Romero et
55 al., 1998b; Llasat and Sempere-Torres, 2001; Llasat et al., 2010; Jansa et al., 2014; Flaounas
56 et al., 2016; Pakalidou and Karacosta, 2018; Amengual et al., 2021). Since 1900, more than
57 500 billion Euros associated with total damages to the property and over 1.3 million fatalities
58 related to hydrometeorological disasters has been registered for the EM-DAT international
59 disaster database¹. These effects underscore the critical need for accurate and rapid high-
60 resolution weather forecasting systems, aimed at extending the lead time for severe weather
61 warnings, thereby enabling the implementation of effective mitigation strategies to reduce
62 fatalities and economic losses. However, while the accuracy of weather forecasting has
63 significantly improved in recent years, with better representation of physical processes and
64 dynamics, accurate prediction of high impact weather events in terms of their location, timing,
65 and intensity remains a major challenge for the scientific community (Stensrud et al., 2009;
66 Mass et al., 2002; Bryan and Rotunno, 2005; Yano et al., 2018; Torcasio et al., 2021). For this
67 reason, improving the forecast of high-impact weather events becomes an imperative goal.

68 Deficiencies in the accurate prediction of the location (spatial and temporal), intensity and
69 phenomenology of extreme weather events are tightly related to the accuracy of the initial
70 conditions of the system (Wu et al., 2013). The initial conditions of the hazardous weather
71 events affecting coastal populated regions, are typically poorly estimated, mainly because these
72 weather systems originate over the sea, where there is a lack of *in-situ* observations. Enhanced
73 representations of the initial conditions are typically achieved by blending information from
74 observations into numerical models through sophisticated *Data Assimilation* (DA) techniques
75 (Kalnay, 2003), which accounts not only for the nominal values of the observations and the
76 model, but also accounts for their respective error statistics. DA has been widely used and
77 applied for global numerical weather prediction (NWP) problems (e.g., Eliassen, 1954; Lorenc,
78 1981; Le Dimet and Talagrand, 1986; Rabier et al., 2000, Whitaker et al., 2008, Carrassi et al.,
79 2018; Albergel, et al., 2020, among others). However, less attention has been paid to
80 convective-scale NWP problems, especially those associated with small scale convective
81 phenomena initiated over regions with sparse observational data coverage, such as the extreme
82 weather events affecting coastal regions in the Mediterranean basin (Carrió et al., 2016;
83 Amengual et al., 2017; Mazzarella et al., 2021). To improve forecasts of such extreme weather
84 events, accurate high resolution numerical weather models which solve convective scale
85 processes are required, as well as dense observations at high spatial and temporal resolution.
86 These will provide accurate information regarding the convective systems themselves or their
87 environmental conditions. One of the most important sources of convective scale information
88 are ground weather radars that provide three-dimensional data related to the storms at high
89 spatial (order of hundreds of meters) and temporal (order of few minutes) resolution. In
90 addition, weather radars provide thermodynamic and dynamic information of thunderstorms,
91 which are crucial to understand and forecast convective structures. Due to the high spatio-
92 temporal variability of convective structures, a rapid update cycle of the initial state (i.e.,

¹ <https://www.emdat.be/>



93 analysis) using weather radar observations is required to reduce errors and keep physical
94 balances in the initial conditions. Several studies have shown the positive impact in forecasting
95 severe weather events by assimilating weather radar information (e.g., Xiao and Sun, 2007;
96 Lee et al., 2010; Wheatley et al., 2012; Yussouf et al., 2015; Carrió et al., 2019; Mazzarella et
97 al., 2021).

98 During the last decades, different DA algorithms have been developed with the aim of
99 improving weather forecasts making use of all available observations in the best possible way.
100 In this context, most of the developed DA methods are based on exploiting Bayes' Theorem
101 (Lorenz, 1986) and making use of different types of approximations. Generally, DA algorithms
102 can be classified into the following three Bayesian-based families: (a) Variational DA (e.g.,
103 3DVar (Barker et al., 2004) or 4DVar (Huang et al., 2009)); (b) Ensemble-based DA, which
104 are based on the *Ensemble Kalman Filter* (EnKF; Evensen, 1994) and (c) Monte-Carlo DA
105 methods. Variational DA minimizes a cost function to obtain the analysis (i.e., the best
106 estimation of the initial conditions). More specifically, variational DA methods provide a
107 (quasi) optimal analysis based on an imperfect forecast (*prior state* or *background*), a set of
108 imperfect observations and their respective error statistics that are prescribed and assumed to
109 be Gaussian, for simplicity. In addition, variational DA algorithms require a linearized and
110 adjoint version of the numerical model, which can be very difficult to develop and maintain.
111 This often involves the use of automatic differentiation tools or complex manual derivation,
112 both of which are error-prone and time-consuming. On the other hand, the ensemble-based DA
113 algorithms do not require the use of linearized or adjoint versions of the model, and they do
114 not use prescribed error statistics. Instead, they compute the error statistics from an ensemble
115 of forecasts, with the main property that these errors are evolving in time as the system evolves.
116 The Monte-Carlo DA method allows the assimilation of observations described with non-
117 Gaussian errors. Particle filters (PF; Van Leeuwen, 2009; Poterjoy, 2016) are a clear example
118 of Monte-Carlo DA algorithm. However, PFs are not well-suited for large multidimensional
119 systems, such as the atmosphere, although a lot of improvements have been achieved recently.
120 In the present study, we will focus on the most widely used DA schemes typically used in major
121 operational weather centers, which are the variational and ensemble-based DA schemes,
122 leaving the Monte-Carlo methods for future work.

123 Although variational DA schemes have been used in numerical weather prediction for many
124 years (Courtier et al., 1994; Park and Zupanski, 2003; Rawlins et al., 2007), allowing the
125 assimilation of a wide range of different observations, they present a well-known limitation.
126 This limitation is related to the use of a climatological background error covariance matrix to
127 characterize the error statistics, which is kept constant along the assimilation window, where
128 the different observations are distributed at different times. This weakness is specifically linked
129 to the 3DVar method, which typically uses the National Meteorological Center (NMC) method
130 (Parrish and Derber, 1992) to generate those static background error covariances using forecast
131 differences over a period of time reasonably close to the event. The error statistics derived from
132 such DA schemes are static, isotropic and nearly homogenous, misrepresenting the true error
133 statistics in space and time, which are inherently flow-dependent, resulting in less accurate
134 analysis. On the other hand, the EnKF DA scheme is designed to provide flow-dependent
135 background error covariances. Some studies have shown the potential of the EnKF spreading
136 information from the observations flow-dependently in comparison with the 3DVar (Yang et
137 al., 2009; Gao et al., 2018). On the other hand, 3DVar techniques require less computational
138 resources and there is no need to build an ensemble compared to EnKF or even simulate the
139 model trajectory as in 4DVar. Therefore, the assimilation with 3DVar takes only a few tens of
140 minutes, making this technique particularly suitable for operational purposes.



141 To solve convective scale (i.e., grid spacing of a few kilometers) physical processes associated
142 with extreme weather phenomena, high-resolution numerical simulations are required.
143 Performing computational expensive high-resolution simulations presents a significant
144 challenge as it constrains the feasible number of ensemble members that can be used in EnKF
145 DA schemes, and thus it could hamper significantly the estimation of the background error
146 covariance matrix. In this context, which DA method is more suitable? The 3DVar using an *ad*
147 *hoc* background error covariance matrix or the low-rank background error covariance matrix
148 obtained from the EnKF?

149 Recently, a few DA studies at convective scale mainly focused just on the mature stage of the
150 weather event have been carried out (e.g., Wheatley et al., 2015; Jones et al., 2016; Yussouf et
151 al., 2020). However, investigating the mature stage means that the weather system is already
152 developed and probably affecting the population. In such situations, the value of improving the
153 atmospheric condition estimation using DA is very limited in terms of lead time, because there
154 is no time left for warning the population and to take actions to reduce socio-economic impacts.
155 In this context, very limited work has been done to assess the impact of DA in pre-convective
156 systems to significantly improve the lead time, allowing warning systems to act as soon as
157 possible. Here, we also investigate the role of the 3DVar and EnKF DA methods in improving
158 pre-convective environment conditions of extreme weather events and how such improved pre-
159 convective conditions could lead to a forecast improvement with significant time in advance to
160 warn the population to take actions.

161 The following study aims at:

162 (a) Assessing the impact of high-resolution 3DVar in comparison with a high-resolution EnKF
163 system to predict small-scale extreme weather events initiated over different areas and with
164 lack of *in-situ* observations.

165 (b) Investigate the potential of using 3DVar and EnKF to enhance the accuracy of atmospheric
166 conditions in the pre-convective environment, hours before the mature stage of convective
167 systems are reached, thereby improving early prediction and warning capabilities for extreme
168 weather events.

169 (c) Quantify the impact of assimilating *in-situ* conventional observations in comparison to
170 assimilating high spatial and temporal resolution data from remote sensing instruments.

171 (d) Provide a quantitative assessment between the different DA schemes by means of using
172 several statistical verification methods.

173

174 It is important to emphasize that this study is not aimed to draw any statistically significant
175 conclusion. Instead, we are interested in comparing the performance of EnKF and 3DVar in
176 two distinct extreme weather events, each with its unique set of conditions and constraints. A
177 heavy rainfall episode affecting coastal regions of Italy during October 2012 (IOP13; Pichelli
178 et al., 2017) and a low-predictable Mediterranean Tropical-like cyclone (medicane) affecting
179 Sicily, known as Qendresa (Pytharoulis et al., 2017; Pytharoulis, 2018; Cioni et al., 2018; Di
180 Muzio et al., 2019), are used for this study.

181 This paper is organized as follows. Section 2 briefly describes the meteorological
182 characteristics of the two events used for comparing the impact of 3DVar and EnKF. In Section
183 3 the observation dataset that will be assimilated by the different DA methods will be presented.



184 Section 4 briefly explains the main characteristics of the two DA algorithms that will be used
185 in this study. Then, the numerical model configuration and the design of the different
186 experiments for the two different case studies will be described in Section 5 and 6, respectively.
187 Section 7 describes the verification methods used in this study. Results of the different
188 numerical experiments for both meteorological situations are summarized in Section 8. Finally,
189 conclusions are presented in Section 9.

190

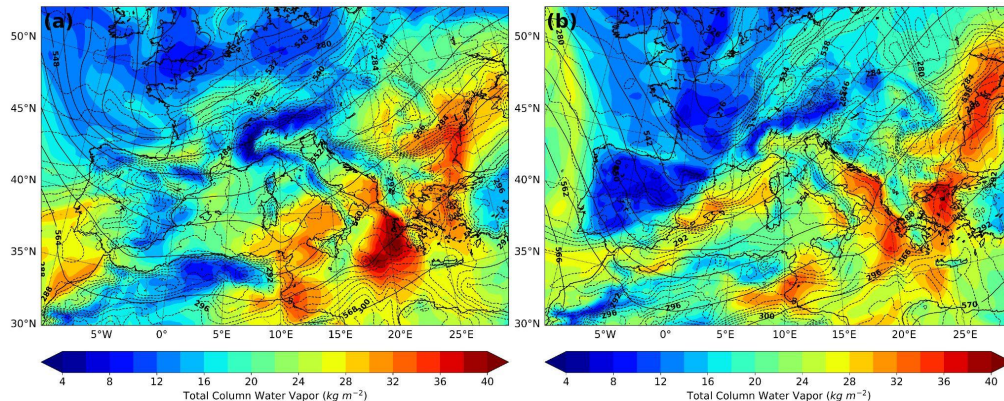
191 **2. Brief Description of Case Studies**

192 Two different extreme weather systems, occurring in the Mediterranean region and affecting
193 populated coastal regions, are considered in this study. The first extreme weather event was
194 associated with heavy rainfall affecting central and northern Italy during October 2012
195 (IOP13), while the second extreme weather event was associated with the Qendresa medicane
196 affecting southern Sicily, Lampedusa, Pantelleria and Malta islands during November 2014.
197 Both systems were poorly forecasted, and for this reason they are perfect candidates for this
198 intercomparison study.

199

200 **2.1. The IOP13 Heavy Precipitation Episode**

201 The *IOP13* occurred during the *First Special Observation Period* (SOP1) of the international
202 project *Hydrological cycle in the Mediterranean Experiment* (HyMeX; Drobinski et al., 2014),
203 that was mainly designed to better understand heavy rainfall and flash flooding episodes
204 occurring in the Mediterranean region. The heavy precipitation IOP13 event took place
205 between 14 and 16 October 2012, and it was characterized by a frontal precipitation system
206 associated with a deep upper-level trough extending from northern France towards northern
207 Spain (Fig. 1). It initially affected southern France coastal areas, and afterward it also affected
208 the northern and central parts of Italy. During 15 October, the Italian rain gauge network
209 registered 24-hour accumulated precipitation with peaks reaching 60 mm in central Italy, 160
210 mm in northeastern Italy and 120 mm in Liguria and Tuscany. During the night of 14 October,
211 a cold front affected the Western Mediterranean region and during 15 October the system
212 rapidly moved from France to Italy, advecting low-level moisture towards the western coast of
213 Italy and Corsica, destabilizing the atmosphere and favoring deep moist convective activity.
214 More details on the synoptic situation and observational data collected during IOP13 can be
215 found in Ferretti et al., 2014.



216
217 Figure 1. IOP13 ERA5 analyses: 500 hPa geopotential (solid black lines), 925 hPa temperature (dashed grey lines)
218 and total column of water vapor (color shaded areas) at (a) 12 UTC 14 October and (b) 00 UTC 15 October 2012.

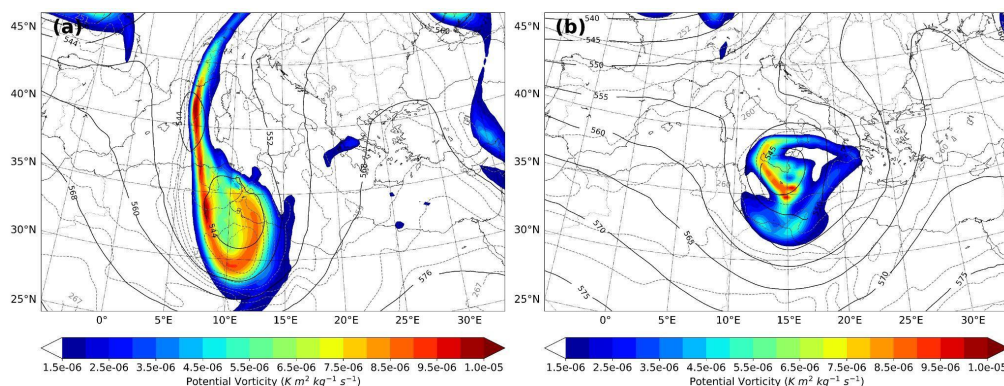
219

220 2.2. The Qendresa Tropical-Like Cyclone Episode

221 Among the wide spectrum of maritime extreme weather events, tropical-like Mediterranean
222 cyclones, a.k.a. medicanes (Emmanuel, 2005), draw particular attention to the community
223 mainly because they share similar morphological characteristics with tropical cyclones. Given
224 their tendency to impact densely populated and economically critical areas around the
225 Mediterranean basin, enhancing the accuracy and reliability of medicanes forecasts has become
226 an urgent priority. Here, we focus on the 7 October 2014 medicanes (Qendresa; Cioni et al.,
227 2018) that affected the islands of Lampedusa, Pantelleria, Malta and the eastern coast of Sicily.
228 This event was recognized by the community for its limited predictability (Carrió et al., 2017),
229 making it a compelling case study for investigating the performance of the 3DVar and EnKF
230 DA methods. *In-situ* observations located in Malta's airport registered gust wind values
231 exceeding 42.7 m s^{-1} and a sudden and deep pressure drop greater than 20 hPa in 6 hours.
232 Satellite imagery during its mature phase showed a well-defined cloud-free eye surrounded by
233 axisymmetric convective activity, which resembles the morphological properties of classic
234 tropical cyclones.

235 A deep upper-level trough associated with a cyclonic flow at mid-levels characterized the
236 synoptic situation in the Western Mediterranean from 5 to 8 November 2014. The upper-level
237 trough was associated with an intense PV streamer extending from Northern Europe to
238 Southern Algeria, and the cyclonic flow at mid-levels was dominated by a strong ridge over
239 the Atlantic and a deep trough moving along Western Europe. Late on 7 November, the upper-
240 level trough became negatively tilted, evolving into a deep upper-level cut-off low and the PV
241 streamer disconnected from the northern nucleus (Fig. 2). A small well-defined spiral-to-
242 circular cloud shape formed just south of Sicily and evolved east-northeastward, reaching its
243 maximum intensity over Malta, at midday. Finally, the cyclonic system dissipated as it crossed
244 the Catania (eastern) coast of Sicily. More details on the synoptic situation and observational
245 data collected during this event can be found in Carrió et al., 2017.

246



247
248
249
250

Figure 2. Qendresa ERA5 analyses: 500 hPa geopotential (solid black lines), 500 hPa temperature (dashed grey lines) and 300 hPa Potential Vorticity (color shaded areas) at (a) 00 UTC 7 November and (b) 00 UTC 8 November 2014.

251

252 3. Observations Description

253 In this study, different sources of remote-sensing and *in-situ* observations were available for
254 the two case studies. Specifically, the following three types of observations were assimilated:
255 (a) *in-situ* conventional data, (b) high temporal and spatial reflectivity data from two Doppler
256 Weather Radars and (c) 3D wind speed and direction data derived from satellites.

257

258 3.1. IOP13 Observations

259 For the IOP13, *in-situ* conventional data and remote sensing observations from two Doppler
260 Weather Radars were available. Moreover, conventional data were obtained from the NOAA's
261 *Meteorological Assimilation Data Ingest System* (MADIS), which has the main advantage of
262 providing high-level quality-controlled data² worldwide. In particular, pressure, temperature,
263 humidity and horizontal wind speed and direction from *in-situ* instruments such as METARs,
264 maritime buoys, rawinsondes and aircrafts (Fig. 3a). In addition to these conventional
265 observations, reflectivity data from two Météo-France polarimetric S-band Doppler Weather
266 Radars, were also available on the Gulf of Genoa. One located in Corsica Island (9.496°E,
267 42.129°N) at 63 m ASL, known as Aleria, and the other located in southern France (4.502°E,
268 43.806°N) at 76 m ASL, known as Nimes (Fig. 3a). These two radars, strategically positioned,
269 ensure a good spatial coverage over the Ligurian Sea, the area where initiation and
270 intensification of deep convection occurred, and provide key information about the 3D
271 structure of the convective systems at high spatial and temporal resolution. The two radars
272 perform 5 and 9 elevation scans every 5 minutes, respectively, and their data are available at
273 the HyMeX's official website (see <https://www.hymex.org>). Specifically, Aleria radar provides
274 data at 5 elevation angles: 0.57°, 0.96°, 1.36°, 3.16° and 4.57° with a mean frequency of 2.8
275 GHz. In comparison, Nimes radar provides data at 9 elevation angles: 0.58°, 1.17°, 1.78°, 2.38°,
276 3.49°, 4.99°, 6.5°, 7.99° and 89.97°, also at the same frequency. It is worth mentioning that
277 Aleria and Nimes radar reflectivity data are provided by the Météo-France operational radar
278 network and undergo rigorous data quality control. This ensures that common radar error
279 sources, such as signal attenuation, ground clutter or beam blocking, are meticulously identified

² See https://madis.ncep.noaa.gov/madis_qc.shtml for further details on the Quality Control techniques used.



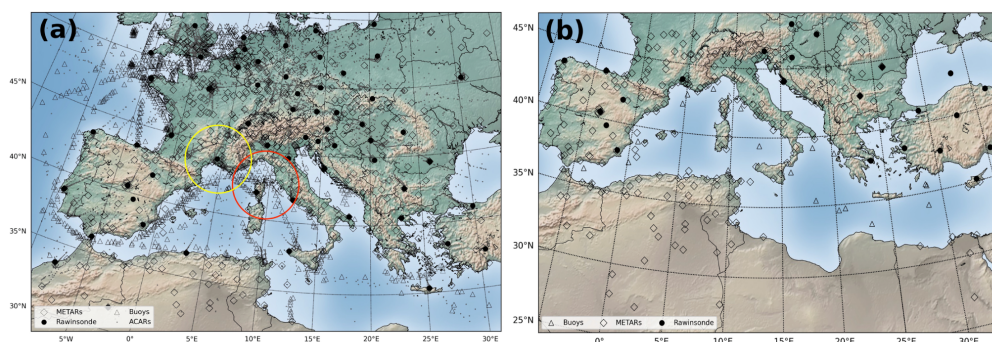
280 and corrected. Radial velocity from Aleria and Nimes Doppler radars was also available, but
281 because of the low reliability of the data (not quality controlled properly) it was not used in this
282 study.

283 Hence, the following observations were assimilated for this event:

- 284 ● Conventional *in-situ* data were hourly assimilated over the entire numerical domain
285 considered (Fig. 3a).
- 286 ● Reflectivity data from two weather radar from Météo-France were assimilated every 15
287 minutes (Fig. 3a).

288 The high spatial resolution of the reflectivity data poses significant challenges for their direct
289 assimilation, potentially leading to detrimental analysis related with signal aliasing and the
290 violation of the uncorrelated observational error assumptions followed in the derivation of the
291 3DVar and EnKF analysis equations. To mitigate the adverse effects associated with these
292 issues, the *Cressman Objective Analysis* technique (Cressman, 1959) was used to interpolate
293 raw radar observations to a regularly spaced 6 km horizontal grid, as suggested by previous
294 work (i.e., Wheatley et al., 2015; Yussouf et al., 2015). It is important to note that reflectivity
295 observations are typically obtained in polar coordinates, a prerequisite step before applying the
296 Cressman interpolation involves converting them to a Cartesian coordinate system. We have
297 performed several sensitivity tests using different grid space resolution (e.g., 3, 6, 9 km) and
298 we found that using 6 km grid space produces the best analysis. To reduce spurious convective
299 signals and remove excessive humidity the *null-echo* option, which allows assimilation of no
300 precipitation echoes, has been adopted in 3DVAR experiment.

301



302 Figure 3. (a) IOP13 Episode: Spatial distribution of *in-situ* observations (gray and black markers) assimilated on
303 the parent numerical domain during 24 h assimilation window from 00 UTC 14 October to 00 UTC 15 October
304 2012. Doppler Weather Radars located at Nimes and Aleria and their coverage range, depicted in yellow and red
305 circles, respectively. (b) Qendresa Episode: Spatial distribution of *in-situ* observations hourly assimilated during
306 12 h assimilation window from 12 UTC 6 November to 00 UTC 7 November 2014.

308

309 3.2. Qendresa Observations

310 For the Qendresa episode, two different observational sources were available: (a) conventional
311 *in-situ* observations and (b) satellite-derived observations. Conventional *in-situ* observations
312 were obtained from MADIS database. However, only observations from buoys, METAR and
313 rawinsonde were used for this case. It is essential to highlight that observation gaps persist

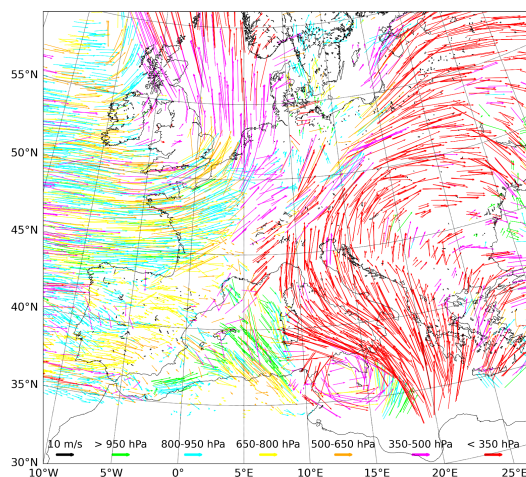


314 across large areas of the region, particularly over the sea (Fig. 3b), where Qendresa initiated
315 and evolved. As for the IOP13, we were interested in Doppler Weather Radars data to enhance
316 the intensity and trajectory forecasts of Qendresa. Unfortunately, Doppler Weather Radars
317 were not available in the neighborhood of the region where Qendresa initiated and evolved,
318 but another source of observations, the so-called *Rapid-Scan Atmospheric Motion Vectors*
319 (RSAMVs; Velden et al., 2017), which provides 3D wind information throughout the entire
320 atmosphere (both speed and direction) at high spatial and temporal resolution (i.e., every 20-
321 min), were available for this event over the sea. This satellite product is obtained using the
322 *Spinning Enhanced Visible and Infrared Imager* (SEVIRI) instrument onboard the *Meteosat*
323 *Second Generation* (MSG) satellite, which has a scanning frequency as low as 5 minutes. The
324 final product is indeed obtained averaging 4 consecutive images.

325 Hence, the following observations were assimilated for this event:

- 326 • Conventional *in-situ* data from buoys, METAR and rawinsonde for the entire
327 Mediterranean region were hourly assimilated.
- 328 • Wind speed and direction from the *Rapid-Scan Atmospheric Motion Vectors* for the
329 entire atmosphere at high spatial and temporal resolution were assimilated every 20
330 minutes.

331 Recent studies have shown that upper-level dynamics played a key role in the genesis and the
332 development of Qendresa (Carrió et al., 2017; Carrió, 2022), so the assimilation of RSAMVs
333 is expected to significantly improve its predictability. Here, the infrared channel from
334 RSAMVs (10.8 μm), which contains information throughout the entire atmosphere, was
335 selected to be assimilated (Fig. 4). However, before assimilating RSAMVs, a quality control
336 check to reject non-physical and outlier observations that could deteriorate the quality of the
337 analysis and the successive forecast was applied. In addition, to minimize the effect of having
338 spatial correlated observation errors associated to high density observations, the “*superobbing*”
339 technique consisting in reducing the data density through spatially averaging the observations
340 within a predefined prism is applied (i.e., Pu et al., (2008); Romine et al., (2013); Honda et al.,
341 (2018)). Based on the most accurate analysis obtained by multiple sensitivity experiments (not
342 shown) for Qendresa, the RSAMVs data are thinned using a prism with horizontal dimensions
343 of 128x128 km² and 25 hPa in the vertical dimension.



344



345 Figure 4. Raw EUMETSAT's RSAMV observations depicted at different vertical levels by infrared channel 10.8
346 μm at 12 UTC on 7 November 2014 over the Mediterranean region. Wind information is only valid at the center
347 of the wind vectors.

348

349 Observations from aircraft (i.e., ACARS) were not assimilated in this case because preliminary
350 assimilation tests indicated a worsening of the results and led to a poorer estimation of the
351 atmospheric state. Buoys, METAR and rawinsonde observations covering the entire
352 Mediterranean region were hourly assimilated.

353 Finally, observational errors used for the assimilation of the observations associated with both
354 IOP13 and Qendresa are motivated by Table 3 in Romine et al., (2013) with the following
355 minor changes: METAR altimeter (1.5 hPa), marine altimeter (1.20 hPa), METAR and marine
356 temperature (1.75 K) and RSAMV wind observations (1.4 m s^{-1}). These minor changes are
357 found to provide better data assimilation analysis for the IOP13 and Qendresa extreme weather
358 events in the Mediterranean region. The remaining of the observation errors are the same as
359 the ones in Romine et al., (2013).

360

361 4. Data Assimilation Schemes

362 In the present study, two widely used data assimilation algorithms are used for improving the
363 forecast of extreme weather events initiated and developed over poorly observed maritime
364 regions and affecting densely populated coastal areas. We refer to the *Ensemble Adjustment*
365 *Kalman Filter* and the variational *3DVar* data assimilation schemes, which are described
366 below.

367

368 a) The Ensemble Adjustment Kalman Filter (EnKF)

369

370 The *Ensemble Adjustment Kalman Filter* (EAKF; Anderson 2001), which is implemented in
371 the *Data Assimilation Testbed Research* (DART³), is used in this study as the former ensemble-
372 based data assimilation technique. The EAKF provides an optimal estimation, in the least
373 square error sense, of the true probability distribution of the state of the atmosphere by merging
374 two main sources of information: (a) the available observations and (b) an ensemble of
375 forecasts (a.k.a. *background*) valid at the analysis time. In particular, the EAKF assimilates the
376 observations serially. This means that the analysis ensemble obtained by the EAKF after the
377 assimilation of the first observation at a given time is then used as the *background* for the next
378 observation at the same analysis time. This is done recursively until all the observations valid
379 at the same analysis time are finally assimilated.

380

381

382

383

³ <http://www.image.ucar.edu/DARes/DART/>



384 In particular, for each observation j from a set of p observations valid at the same analysis time,
 385 the EAKF can be summarized with the 4 main steps described below:

386

387 **Step 1)** Obtain the observed value y_j^o , and the associated observation error variance, R_{jj}

388 **Step 2)** Update the ensemble mean $\langle y_j^f \rangle$ and ensemble members y_j^f of the observed variable
 389 using:

$$\langle y_j^a \rangle = \langle y_j^f \rangle + \frac{H_j Z (H_j Z)^T}{H_j Z (H_j Z)^T + R_{jj}} (y_j^o - \langle y_j^f \rangle) = \langle y_j^f \rangle + \frac{H_j \mathbf{P}^f H_j^T}{H_j \mathbf{P}^f H_j^T + R_{jj}} (y_j^o - \langle y_j^f \rangle) \quad (\text{Eq. 1})$$

390 $y_{ji}^a = y_{ji}^f + \sqrt{[1 - P^f (P^f + R_{jj})^{-1}]} (y_{ji}^f - \langle y_j^f \rangle);$ for $i=1, \dots, K$ and $P^f = H_j P^f H_j^T$ (Eq. 2)

391 where $y_{ji}^f = H_j(\mathbf{x}_i^f)$; $\langle y_j^f \rangle = \frac{1}{K} \sum_{i=1}^K H_j(\mathbf{x}_i^f)$; $H_j Z = \frac{1}{\sqrt{K-1}} [y_{j1}^f - \langle y_j^f \rangle, \dots, y_{jK}^f - \langle y_j^f \rangle]$

392

393 **Step 3)** Find corresponding analysis ensemble for the observations and model variables using
 394 a linear regression step:

$$y_{ki}^a = y_{ki}^f + \frac{H_k Z (H_k Z)^T}{H_k Z (H_k Z)^T + R_{jj}} (y_{ji}^a - y_{ji}^f), \text{ for } k=1, \dots, p \text{ and } i=1, \dots, K \quad (\text{Eq. 3})$$

395 $x_{\mu i}^a = x_{\mu i}^f + \frac{Z(\mu, :) (H_j Z)^T}{H_k Z (H_j Z)^T + R_{jj}} (y_{ji}^a - y_{ji}^f),$ for $\mu=1, \dots, n$ and $i=1, \dots, K$ (Eq. 4)

396 where n is the number of model variables.

397 **Step 4)** Let the analysis ensemble become the background ensemble for the next observation:

$$y_{ki}^f = y_{ki}^a, \text{ for } k=1, \dots, p \text{ and } i=1, \dots, K \quad (\text{Eq. 5})$$

398 $x_{\mu i}^f = x_{\mu i}^a,$ for $\mu=1, \dots, n$ and $i=1, \dots, K$ (Eq. 6)

399 In the above equations, K is the number of ensemble members, p the number of observations,
 400 n is the number of model variables, H is the observation operator (non-linear) and Z the
 401 ensemble perturbations about the mean. The superscripts “ a ” and “ f ” stand for the analysis and
 402 forecast, respectively.

403 Ensemble covariances used in high-resolution simulations, such as the present study, where
 404 only a limited number of ensemble members is feasible, suffers from sampling error, resulting
 405 in the generation of spurious correlations that hamper the analysis (Hacker et al., 2007). The
 406 detrimental effects of these spurious correlations are mitigated by employing covariance
 407 localization functions that go to zero as the distance between the assimilated observation and
 408 the grid model point where the analysis occurs, increases (Houtekamer and Mitchell, 1998). In
 409 our case, a fifth-order piece-wise rational Gaussian localization function is used (Gaspari and



410 Cohn, 1999). For this study, after several sensitivity simulations it was found that using a half-
411 radius⁴ of 230 km in the horizontal and a half-radius of 4 km in the vertical for the horizontal
412 and vertical localizations, respectively, results in the best performance of the DA scheme.

413 The assimilation of each observation results in a reduction of the ensemble spread, attributed
414 to using a reduced-moderate ensemble size (Anderson and Anderson, 1999). To address this
415 issue and help to maintain the spread, an *adaptive inflation technique* (Anderson and Collins,
416 2007; Anderson et al., 2009) is applied to the prior ensemble before assimilating the
417 observations. The adaptive inflation technique increases the spread of the ensemble without
418 changing the mean. The inflation value has a probability density distribution described by a
419 mean and a standard deviation. In this study, it was determined that initializing the mean value
420 of inflation at 1.0 and using a standard deviation of 0.6, yields the best performance of the DA
421 scheme.

422

423 **b) Three-dimensional Variational Data Assimilation (3DVar)**

424 The 3DVar technique, implemented in WRFDA (Barker et al., 2004), is adopted for the
425 numerical simulations. The 3DVar aims to seek the best estimate of the initial conditions
426 through the iterative minimization of a cost function:

$$427 \quad J(\mathbf{x}) = \frac{1}{2} \left\{ (\mathbf{x} - \mathbf{x}_b)^T \mathbf{B}^{-1} (\mathbf{x} - \mathbf{x}_b) + [\mathbf{y}_o - \mathbf{H}(\mathbf{x})]^T \mathbf{R}^{-1} [\mathbf{y}_o - \mathbf{H}(\mathbf{x})] \right\} \quad (\text{Eq.7})$$

428 where \mathbf{B} and \mathbf{R} are the background and observation error matrices, respectively; \mathbf{x} is the state
429 vector; \mathbf{y}_o is the observations, \mathbf{x}_b is the first guess and H is the forward (non-linear) operator
430 that converts data from model space to observation space.

431 The solution of the above cost function J consists in finding a state \mathbf{x}_a (analysis), that minimizes
432 the distance between the observations and the background field. However, in a model with 10^6
433 degrees of freedom, the direct solution is computationally expensive. To reduce the complexity
434 and calculate \mathbf{B}^{-1} more efficiently, a pre-conditioning is applied by transforming the control
435 variables, respectively, pseudo relative humidity, temperature, u , v , and surface pressure, as \mathbf{x}
436 $- \mathbf{x}_b = \mathbf{U}\mathbf{v}$, where \mathbf{v} is the control variable and \mathbf{U} the transformation operator.

437 Regarding the assimilation of radar reflectivity, the observation operator from Sun and Crook
438 (1997) is adopted:

$$439 \quad Z = a + b \log_{10}(\rho q_r) \quad (\text{Eq. 8})$$

440 where Z is the reflectivity, q_r is the rainwater mixing ratio, ρ the air density whereas the
441 coefficients a and b are equal to 43.1 and 17.5, respectively.

442

443 The background error covariance matrix \mathbf{B} matrix plays a key role in the assimilation process
444 by weighing and smoothing the information from observations and by ensuring a proper
445 balance between the analysis fields. The *National Meteorological Center* method (NMC;
446 Parrish and Derber, 1992) was used to model the \mathbf{B} matrix. This method evaluates the

⁴ The half-radius or cutoff term is defined here as 0.5 times the distance to where the impact of the observation assimilated go to zero. Multiplying the half-radius by 2 results in the maximum distance at which an observation can modify the model state.



447 differences, over a period of two weeks, between two short-term forecasts valid at the same
448 time but with different lead time, 12h and 24h, respectively, to generate the forecast error
449 covariance matrix **B**. Recently, several works (Wang et al., 2013; Li et al., 2016; Shen et al.,
450 2022; Ferrer Hernandez et al., 2022) show the benefit of using a slightly different approach for
451 the **B** matrix (CV7) in assimilating radar reflectivity, besides in precipitation forecast accuracy.
452 The CV7 differs from the others by using empirical orthogonal functions (EOFs) to represent
453 the vertical covariance instead of a vertical recursive filter. Moreover, the control variables are
454 in eigenvector space, and they are the following: u, v, temperature, pseudo relative humidity
455 (RH_s), and surface pressure (P_s). Therefore, CV7 option has been used to generate the **B** matrix
456 for both case studies. In this study, the weak penalty constraint (WPEC) option (Li et al., 2015)
457 implemented in WRFDA has been activated to improve the balance between the wind and
458 thermodynamic state variables, enforcing the quasi-gradient balance on the analysis field.

459

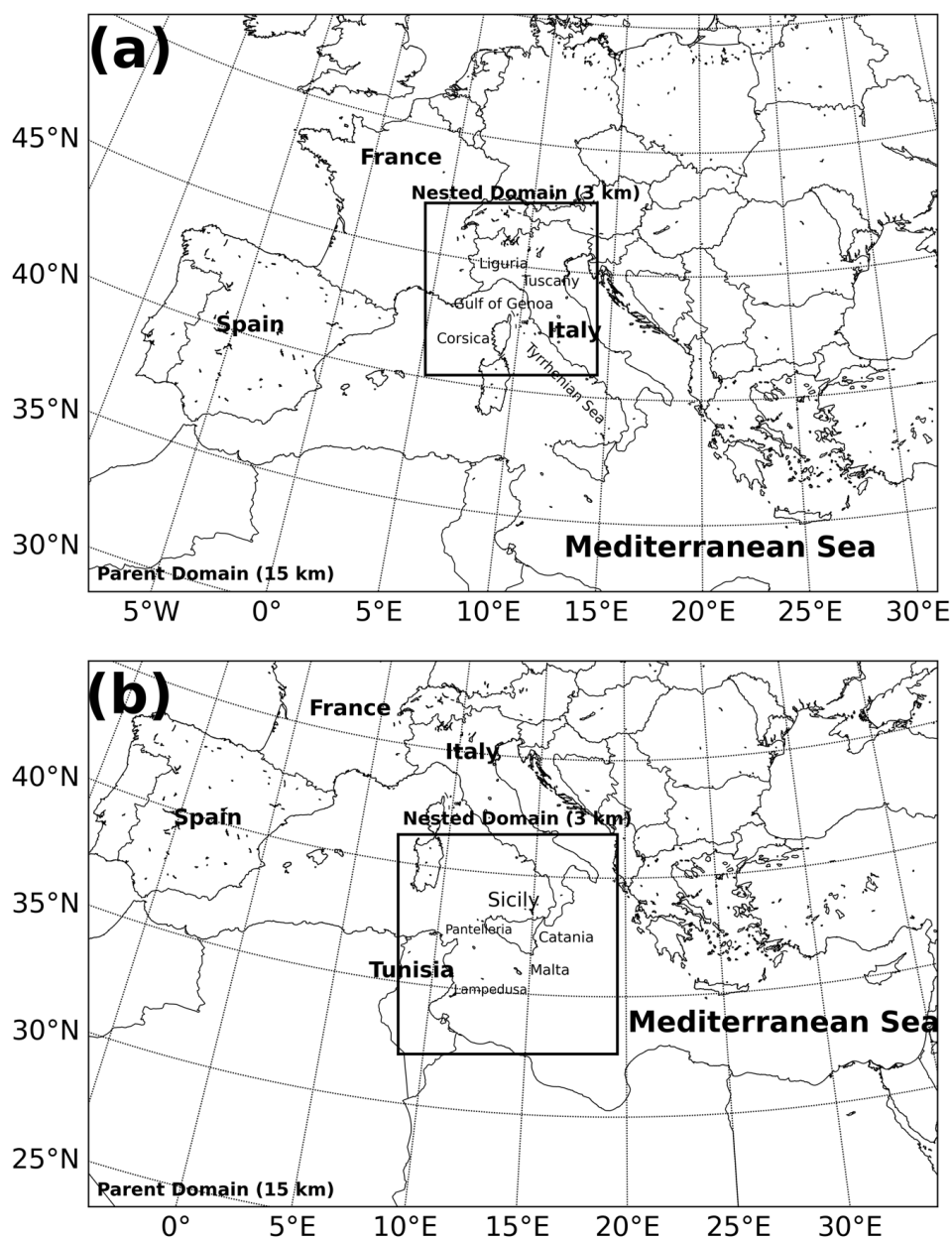
460 5. Model set-up

461 The mesoscale Advanced Research Weather Research and Forecasting Model (WRF;
462 Skamarock et al., 2008) version 3.7 is used in this study. WRF solves a fully compressible and
463 non-hydrostatic set of equations, using a η terrain-following hydrostatic-pressure vertical
464 coordinate. The Arakawa C-grid staggering scheme and a third-order Runge-Kutta time-
465 integration, to improve the precision of the numerical solutions, are used. Because IOP13 and
466 Qendresa episodes took place in different locations and with different conditions, two different
467 model configurations were used. For the IOP13 episode, a one-way nested model configuration
468 with the parent domain centered over the Western Mediterranean Sea, covering Central Europe
469 and North Africa, with a horizontal grid-resolution of 15 km (168x247) and a nested domain
470 centered over Gulf of Genoa with a horizontal grid-resolution of 3 km (250x250) were used
471 (Fig. 5a). Both domains were characterized to have 51 vertical model levels, from surface to
472 50 hPa, with higher density of levels in the lower part of the atmosphere than in the upper. For
473 Qendresa, a two one-way nested model configuration is also used, but now the parent domain
474 is centered over the Central Mediterranean Sea, covering most of the European region and the
475 northern part of Africa (Fig. 5b), using a horizontal grid resolution of 15 km (245x245). The
476 nested domain is centered over Sicily (Southern Italy) using a grid resolution of 3 km
477 (253x253). Both numerical domains use a 51 terrain-following η levels up to 50 hPa, as in the
478 IOP13 case.

479 For the EnKF DA experiments, initial and boundary conditions used to perform the simulations
480 associated with IOP13 were obtained from the *European Center of Medium Range Weather*
481 *Forecasts Global Ensemble Prediction System* (EPS-ECMWF), which stored meteorological
482 fields using a horizontal and vertical spectral triangular truncation of T639L62 (i.e., ~32 km
483 grid resolution in the horizontal). In particular, the EPS-ECMWF provides 51 different initial
484 and boundary conditions from 50 perturbed ensemble members plus a control simulation.
485 However, due to unfeasible computational resources required to run our numerical simulations
486 at high grid resolution, here we will use an ensemble consisting of 36 members. This
487 configuration is analogous to the one used at the internationally prestigious *National Oceanic*
488 *and Atmospheric Administration - National Severe Storms Laboratory* (NOAA-NSSL) in
489 Norman (Oklahoma, USA) to improve predictability of tornadoes. To obtain the desired 36-
490 member ensemble, a *Principal Components Analysis* and *K-mean* clustering technique were
491 used together to select the 36 ensemble members from the EPS-ECMWF showing more
492 dispersion over the entire numerical domain (see Garcies and Homar, 2009 and Carrió et al.,
493 2016 for more details using these techniques). To perform Qendresa DA simulations, the initial



494 and boundary conditions were obtained following the same methodology explained above for
495 the IOP13 case, i.e., using an ensemble of 36 members obtained from the EPS-ECMWF. On
496 the other hand, the initial and boundary conditions for 3DVar simulations are provided by the
497 *Integrated Forecast System* (IFS) global model from the ECMWF, with a spatial resolution of
498 $0.1^\circ \times 0.1^\circ$ and updated every 3 hours.



499 Figure 5. Mesoscale and storm-scale numerical domains used in this study for the (a) IOP13 and (b) Qendresa
500 episodes, respectively.
501



502

503 To estimate the uncertainties of WRF, which is a necessary information for the EnKF, a
 504 multiphysics ensemble is built for both the IOP13 and Qendresa event (e.g., Stensrud et al.,
 505 (2000); Wheatley et al., (2012)), where each ensemble member gets a different set of
 506 parameterizations (see Table 1). In particular, the diversity in our ensemble consists of (a) two
 507 short- and long-wave radiation schemes [Dudhia (Dudhia, 1989) and RRTMG (Iacono et al.,
 508 2008)], (b) three cumulus parameterizations schemes [Kain-Fritsch (KF; Kain and Fritsch,
 509 1993; Kain, 2004), Tiedtke (Tiedtke, 1989) and Grell-Freitas (GF; Grell and Freitas, 2013)]
 510 and (c) three planetary boundary layer schemes [Yonsei University (YSU; Hong et al., 2006),
 511 Mellor-Yamada-Janjic (MYJ; Janjic, 1990, 2001), and Mellor-Yamada-Nakanishi-Niino level
 512 2.5 (MYNN2; Nakanishi and Niño, 2006, 2009)]. Two widely used physics parameterizations
 513 are adopted for the microphysical processes and land surface interactions, the New Thompson
 514 (Thompson et al., 2008) and Noah (Tewari et al., 2004) schemes, respectively. Note that the
 515 above-mentioned physical parameterizations are used for both the large-scale ensemble in the
 516 parent domain and the storm-scale ensemble in the nested domain, except for the cumulus
 517 parameterization that is only applied in the parent domain ensemble. On the other hand, for the
 518 WRF deterministic simulation using 3DVar, the microphysical processes are parametrized by
 519 using the New Thompson scheme, while a YSU scheme is adopted for PBL. Long- and short-
 520 wave radiation are considered through a RRTMG and Dudhia scheme, respectively; while
 521 Kain-Fritsch scheme is used for the convection, except for the inner domain where it is
 522 explicitly resolved.

523

524 **Table 1:** Multiphysics parameterizations used to generate the 36-member ensemble for the EnKF experiments in
 525 IOP13 and Qendresa episodes. PBL, SW and LW stand for planetary boundary layer, short-wave and long-wave,
 526 respectively.

Multiphysic Configuration											
Ens. Memb.	MP	CU	PBL	Land Sfc	SW/LW Rad.	Ens. Memb.	MP	CU	PBL	Land Sfc	SW/LW Rad.
1	New Thompson	KF	YSU	Noah	Dudhia	19	New Thompson	KF	YSU	Noah	Dudhia
2	New Thompson	KF	YSU	Noah	RRTMG	20	New Thompson	KF	YSU	Noah	RRTMG
3	New Thompson	KF	MYJ	Noah	Dudhia	21	New Thompson	KF	MYJ	Noah	Dudhia
4	New Thompson	KF	MYJ	Noah	RRTMG	22	New Thompson	KF	MYJ	Noah	RRTMG
5	New Thompson	KF	MYNN2	Noah	Dudhia	23	New Thompson	KF	MYNN2	Noah	Dudhia
6	New Thompson	KF	MYNN2	Noah	RRTMG	24	New Thompson	KF	MYNN2	Noah	RRTMG
7	New Thompson	GF	YSU	Noah	Dudhia	25	New Thompson	GF	YSU	Noah	Dudhia
8	New Thompson	GF	YSU	Noah	RRTMG	26	New Thompson	GF	YSU	Noah	RRTMG
9	New Thompson	GF	MYJ	Noah	Dudhia	27	New Thompson	GF	MYJ	Noah	Dudhia



10	New Thompson	GF	MYJ	Noah	RRTMG	28	New Thompson	GF	MYJ	Noah	RRTMG
11	New Thompson	GF	MYNN2	Noah	Dudhia	29	New Thompson	GF	MYNN2	Noah	Dudhia
12	New Thompson	GF	MYNN2	Noah	RRTMG	30	New Thompson	GF	MYNN2	Noah	RRTMG
13	New Thompson	Tiedke	YSU	Noah	Dudhia	31	New Thompson	Tiedke	YSU	Noah	Dudhia
14	New Thompson	Tiedke	YSU	Noah	RRTMG	32	New Thompson	Tiedke	YSU	Noah	RRTMG
15	New Thompson	Tiedke	MYJ	Noah	Dudhia	33	New Thompson	Tiedke	MYJ	Noah	Dudhia
16	New Thompson	Tiedke	MYJ	Noah	RRTMG	34	New Thompson	Tiedke	MYJ	Noah	RRTMG
17	New Thompson	Tiedke	MYNN2	Noah	Dudhia	35	New Thompson	Tiedke	MYNN2	Noah	Dudhia
18	New Thompson	Tiedke	MYNN2	Noah	RRTMG	36	New Thompson	Tiedke	MYNN2	Noah	RRTMG

527

528 6. Design of IOP13 and Qendresa Experiments

529 To quantitatively assess the benefits of assimilating different types of observations using the
 530 3DVar and the EnKF DA schemes, a few numerical experiments are performed. A reference
 531 experiment without any data assimilation is carried out. Then, several numerical experiments
 532 using different types of observations for the assimilation are performed. Only conventional *in-*
 533 *situ* observations are assimilated using the 3DVar and the EnKF, for the first set of experiments.
 534 All available observations (i.e., conventional, radar based and satellite derived data) are
 535 assimilated using both 3DVar and EnKF, for the second type of experiments. The comparison
 536 between these numerical experiments will provide information on which DA scheme and
 537 observation is performing better for these weather events. The DA experiments mainly consist
 538 of two phases: the first one is related to the data assimilation procedure, where different types
 539 of observations are assimilated by the variational 3DVar and the ensemble-based EnKF DA
 540 schemes; the second phase is associated with the free model run initialized using the initial
 541 conditions obtained during the first phase. The total forecast time is 24 h and 36 h for IOP13
 542 and Qendresa, respectively. For IOP13, a further simulation lasting 6-hour from 18 UTC 13
 543 October to 00 UTC 14 October 2012 (Carrió et al., 2019) is performed (Fig. 6) to reduce spin-
 544 up problems related to the direct downscaling from global ECMWF analysis (32 km grid
 545 resolution) to the WRF parent domain used in our simulations (16 km grid resolution). This
 546 procedure improved the DA for IOP13, but it had a small impact for Qendresa.

547 Therefore, the following model simulations were performed:

- 548 ● No Data Assimilation (NODA)
- 549 ● Only conventional *in-situ* observations are assimilated using the 3DVar and the EnKF
 550 (SYN)
- 551 ● All available observations (i.e., conventional, radar based and satellite derived data) are
 552 assimilated using both 3DVar and EnKF (CNTRL)



553 The comparison between SYN and CNTRL will allow for assessing the role of radar and/or
554 satellite data, especially for the events originated in the area where observations are not
555 available. Moreover, the assimilation of the radar and/or satellite will produce important
556 information on the triggering phase of both events developing on the sea.

557

558 6.1. CNTRL Experiments

559 For IOP13, the CNTRL experiment is designed to assimilate both *in-situ* conventional and
560 reflectivity observations from Aleria and Nimes Doppler weather radars. The assimilation of
561 the reflectivity is expected to improve the forecast of this event by significantly improving the
562 initial conditions over the sea, where convective activity initiated and evolved into deep
563 convection affecting coastal populated areas of Italy. As briefly described in the previous
564 section, this experiment consists of three stages: 1) the spin-up of the storm-scale domain is
565 accounted for by running the WRF model during 6 hours from 18 UTC 13 October to 00 UTC
566 14 October 2021. Note that for the 3DVar experiment, the spin-up is accounted by just
567 initializing WRF with the deterministic analysis from the IFS ECMWF. However, for the EnKF
568 counterpart, the spin-up is accounted by initializing the 36-member ensemble at 18 UTC 13
569 October; 2) *in-situ* conventional observations were hourly assimilated during 24 hours from 00
570 UTC 14 October to 00 UTC 15 October, meanwhile reflectivity observations were assimilated
571 using a Rapid-Update Assimilation Cycle every 15 minutes during a period of 6 hours, from
572 18 UTC 14 October to 00 UTC 15 October (Fig. 6b); and 3) a 24-h ensemble (deterministic)
573 forecast until 00 UTC 16 October, using the recently obtained initial conditions, is performed
574 by the EnKF (3DVar).

575 For the Qendresa episode, CNTRL experiment is designed to assimilate both *in-situ*
576 conventional and RSAMV observations. The assimilation of RSAMV observations is expected
577 to improve the representation of the atmospheric circulation at upper-levels, whereas the
578 assimilation of surface conventional observations is expected to enhance the one at low-levels.
579 The Qendresa CNTRL experiment consists of two main phases: 1) *in-situ* conventional and
580 satellite derived RSAMV observations are hourly and 20-min assimilated, respectively, during
581 a 12-h period from 12 UTC 6 November to 00 UTC 7 November 2014 to end up with the last
582 analysis at the end of the assimilation window (i.e., 00 UTC 7 November); 2) a free 36-h
583 ensemble (deterministic) forecast is performed by the EnKF (3DVar) from 00 UTC 7
584 November to 12 UTC 8 November 2014 (Fig. 6e).

585

586 6.2. SYN Experiments

587 For IOP13, the SYN experiment assesses the impact of *in-situ* conventional observations,
588 which are crucial to characterize mesoscale atmospheric circulation. Analogous to the CNTRL,
589 SYN follows the same three phases, but in the second phase only the hourly *in-situ*
590 conventional observations from 00 UTC 14 October to 00 UTC 15 October 2012 are
591 assimilated. The analysis obtained from the assimilation stage is used as initial conditions for
592 running the free forecast for 24h, in the third phase (Fig. 6a).

593 Similarly, also for Qendresa, in the SYN experiment only *in-situ* conventional observations are
594 hourly assimilated for 12 hours, from 12 UTC 6 November to 00 UTC 7 November 2014 (Fig.
595 6d).

596

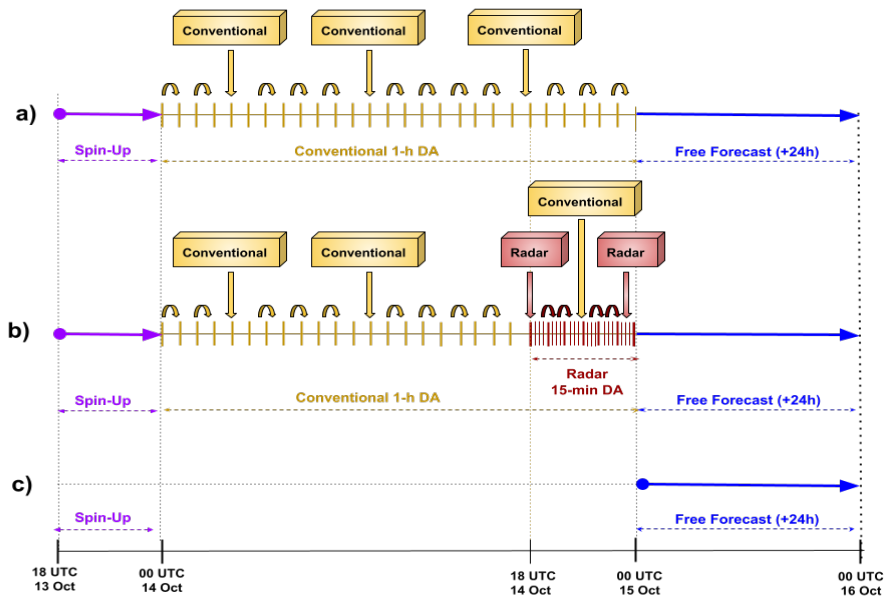


597

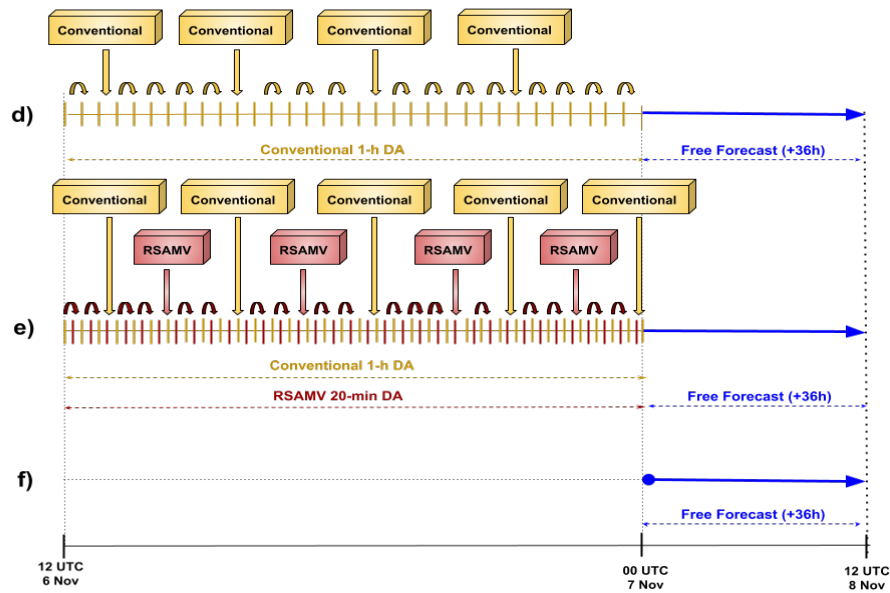
598 6.3. NODA Experiments

599 For the IOP13, NODA experiment is a direct downscaling from EPS-ECMWF boundary and
600 initial conditions valid at 00 UTC 15 October to 00 UTC 16 October 2012. To the aim of
601 simulating an operational framework, the NODA experiment starts at 00 UTC 15 October,
602 instead of starting at 18 UTC 14 October (Fig. 6c). With this choice of the starting time, one
603 could answer the question of which forecast system we should use to predict a 24-48 h forecast.
604 Should we simply perform a simple downscaling using the last analysis obtained from a global
605 model, or should we start our simulation with a previous analysis but now using DA at high
606 temporal and spatial resolution to enhance the estimation of the initial conditions? The
607 comparison among NODA, CNTRL and SYN will provide us with valuable information on the
608 impact of assimilating different sources of observations.

609 For Qendresa, NODA experiment is simply a direct downscaling of 36 hours from EPS-
610 ECMWF at 00 UTC 7 November to 12 UTC 8 November 2014 (Fig. 6f). Here again, it is
611 important to note that the choice of starting NODA at 00 UTC 7 November instead of starting
612 at 12 UTC 6 November was made intentionally to extract general conclusions applicable to an
613 operational framework.



614



615

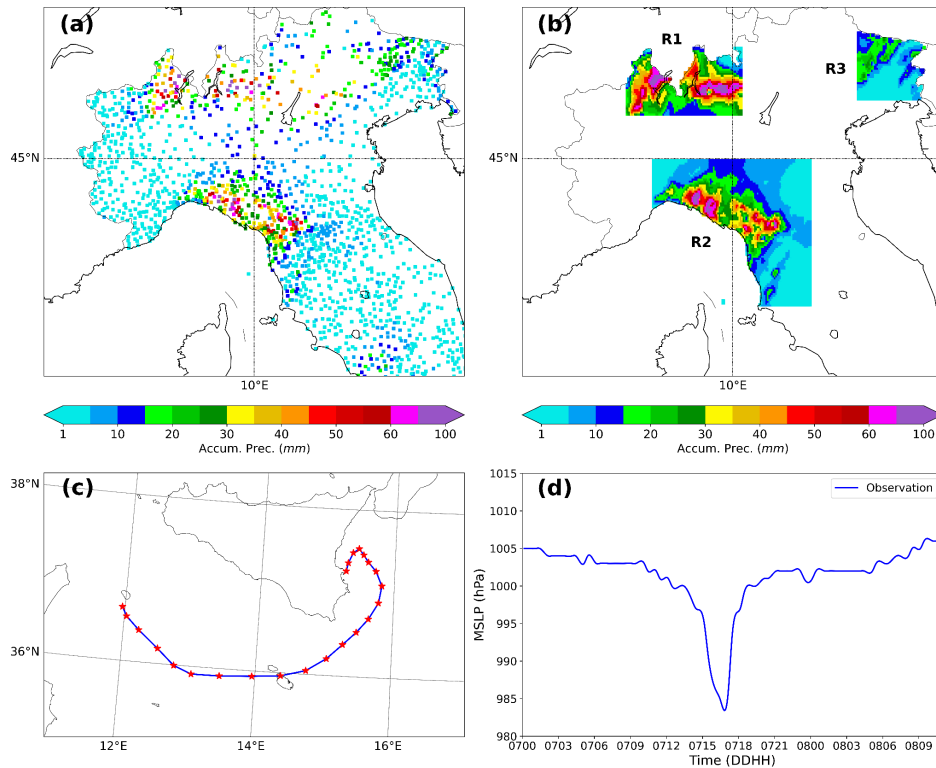
616 Figure 6. Schematic representation of the main numerical experiments performed in this study for the IOP13 and
617 Qendresa episodes, respectively. SYN, CNTRL and NODA experiments for the IOP13 are shown in (a), (b) and
618 (c) panels, respectively, meanwhile the ones corresponding to Qendresa are shown in (d), (e) and (f), respectively.

619

620 7. Verification Methods

621 To quantitatively evaluate the performance of the EnKF and the 3DVar and their impact on the
622 short-term forecasting of these two extreme weather events, various verification scores are
623 used. Given the different nature of the weather phenomena associated with these episodes, the
624 selection of verification scores is tailored specifically to each event. For the IOP13 heavy
625 precipitation event (Fig. 7a), the model verification was performed using the observed
626 accumulated precipitation field over different time windows (e.g., 3 hours, 6 hours or 9 hours).
627 More specifically, the accumulated precipitation was computed using observations from the
628 *Italian Department of Civil Protection*. However, the spatial distribution of rain gauges is not
629 homogenous and there are regions where a lack of rain gauges is present. To address these
630 issues, three sub-regions are chosen where the heavy precipitation event was well recorded by
631 the weather stations (see R1, R2 and R3 in Fig. 7b). Conversely, for the Qendresa tropical-like
632 cyclone, a limited number of *in-situ* observations were present since it initiated and moved over
633 the sea during its lifecycle, and radar-data were not available. Consequently, IR satellite
634 imagery was the primary source of data to approximately estimate Qendresa's trajectory (Fig.
635 7c). Regarding the intensity of Qendresa, since the cyclone's center passed over Malta island,
636 reaching its minimum mean sea level pressure (MSLP) of 985 hPa, METAR data from Malta's
637 airport was also used to verify the cyclone's intensity (Fig. 7d).

638



639
640 Figure 7. (a) Example of the 12-h accumulated precipitation estimated values and their spatial distribution from
641 the *Italian Department of Civil Protection* rain gauges. (b) Linear interpolation of 12-h accumulated precipitation
642 values into the three target areas where verification has been performed. (c) Observed track of Qendresa medicane
643 viewed from infrared satellite imagery. (d) Surface pressure (hPa) data obtained from the METAR station at
644 Malta's airport.

645

646 To quantitatively assess the short-term (i.e., first 6-9 hours) precipitation forecast for the IOP13
647 initialized using the analysis from the 3DVar and EnKF DA techniques, the *Filtering Method*,
648 the *Relative Operating Characteristics* (ROC; Mason, 1982; Stanski et al., 1989; Swets, 1973)
649 and the *Taylor Diagrams* (Taylor, 2001) were used. We avoid using the conventional point-
650 by-point approach, which has been shown to have serious limitations in the evaluation of high-
651 grid spatial and temporal precipitation field resolutions (Roberts, 2003). More specifically, as
652 *Filtering Method* we use the *Fraction Skill Score* (FSS; Roberts and Lean, 2008), which is
653 commonly used to quantitatively assess precipitation. A preliminary interpolation of the
654 forecast and the observations onto a common regular mesh of 3 km is performed to compute
655 FSS. Then the comparison is carried out within a region of 3x3 grid cells around each grid cell.
656 The FSS can be used to determine the scale over which a forecast system has sufficient skill
657 (Mittermaier, 2010). The FSS ranges from 0 to 1, being 1 a perfect match between model and
658 observations. In addition to the ROC curves, the *Area Under the ROC Curve* (AUC; Stanski
659 et al., 1989; Schwartz et al., 2010), which is also widely used to quantitatively assess the quality
660 of weather forecasts, will be also used in this study. For a perfect forecast, AUC is equal to 1.

661 For Qendresa, the *Whisker diagrams* (Tukey, 1977) and the *Probability Distribution of the*
662 *Cyclone Center Occurrence* (PCCO), which was based on the *Kernel Density Estimation*



663 (KDE; Bowman and Azzalini, 1997; Scott, 2015; Silverman, 2018), were used to validate the
664 simulations. More specifically, the KDE is used to compute the probability of having the center
665 of the cyclone over the entire numerical domain. The main idea behind KDE is to place a
666 “kernel” (i.e., a probability distribution function) at each data point, and then sum up the kernels
667 to estimate the overall probability density function. The kernel is typically chosen to be a
668 smooth function, such as a Gaussian, that decays to zero as the distance from the data point
669 increases. The width of the kernel is controlled by a parameter called the bandwidth, which it
670 turns out to be one of the limitations of the KDE technique. In this case, we found that the
671 optimal bandwidth is 20 km, which is within the meso β scale, i.e. a typical length scale for
672 convective cells. Here, a 2-dimensional KDE will be applied over each cyclone center (*lat, lon*
673 coordinates) identified for the different simulations (i.e., EnKF vs 3DVar). In this way, we will
674 infer the most probable track of Qendresa for the different simulations, thereby identifying
675 which is the best DA technique and which provides better estimations of Qendresa medicane’s
676 track.

677

678 8. Results

679 To quantitatively estimate the impact on the short-range forecast from assimilating the different
680 types of observations considered in this study, using the 3DVar and the EnKF, the
681 abovementioned verification techniques were applied for the two extreme events. Because of
682 the differences in their features, we used the *Filtering method*, the *Relative Operating*
683 *Characteristics (ROC)* and *Area Under the ROC curve* and the *Taylor diagrams* for IOP13,
684 and the *Whisker diagrams* and the *Probability Distribution of Cyclone Center Occurrence* for
685 Qendresa. The results are described in the following subsections.

686

687 8.1. Statistical analysis: IOP13 Episode

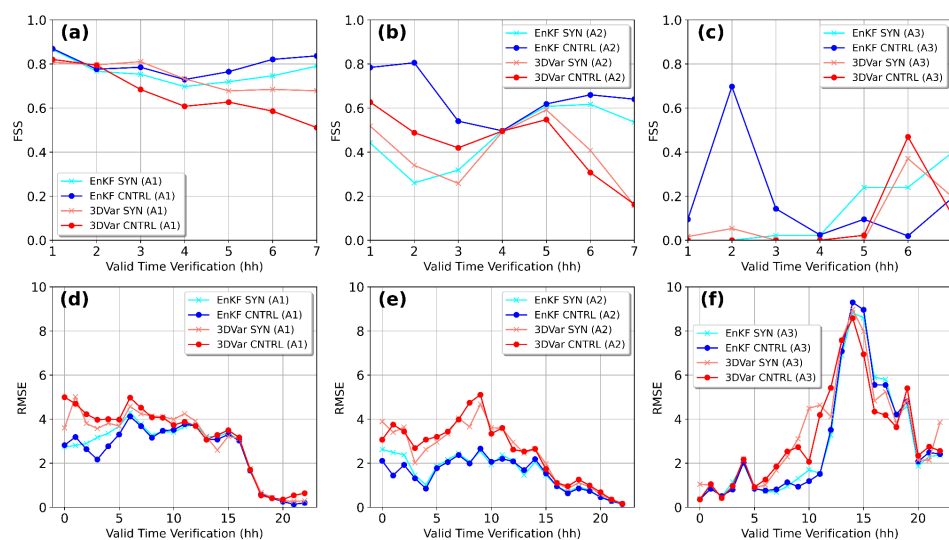
688 Because IOP13 was a heavy rainfall episode, to quantitatively assess the impact on the short-
689 range forecasts from assimilating both *in-situ* conventional and reflectivity observations from
690 Doppler weather radars using the 3DVar and the EnKF DA algorithms, the accumulated
691 precipitation field will be used here.

692

693 8.1.1. Filtering Method

694 The FSS associated with the accumulated precipitation field is computed independently for the
695 three sub-regions R1, R2 and R3 highlighted in Fig. 7b, where the density of observation was
696 higher, using as threshold $1 \text{ mm}\cdot\text{h}^{-1}$. In general, the comparison in terms of FSS (Fig. 8 a-c)
697 shows that EnKF outperforms 3DVar during the first 7 hours of free forecast in the three sub-
698 regions. As it was expected, the CNTRL experiments for both the EnKF and 3DVar outperform
699 the SYN experiments, where reflectivity observations were not considered. Moreover, Fig. 8a
700 shows that the 3DVar-CNTRL provides the worst scores, except for the first few hours of
701 simulation where 3DVar-CNTRL performs better than 3DVar-SYN. This is because the
702 information ingested from the radar using the 3DVar in that region is lasting no longer than 2
703 hours. Something similar happens with the EnKF after 4 hours. These results would agree with
704 past studies, showing similar behaviors (Carrió et al., 2016; Carrió et al., 2019).

705



706
707
708 Figure 8. Upper panels: Evolution of the FSS during the first 7 hours of free forecast in the Italian sub-regions (a)
709 R1, (b) R2 and (c) R3, using a threshold $> 1 \text{ mm}\cdot\text{h}^{-1}$. Lower panels: Evolution of the RMSE during the first 24
710 hours of free forecast in the sub-regions (d) R1, (e) R2 and (f) R3. Simulations assimilating both conventional and
711 radar observations (CNTRL) and simulations assimilating only conventional observations (SYN) associated with
the 3DVar and the EnKF are shown here.

712

713 In addition to the FSS, we also compute the typical and widely used root-mean-squared-error
714 (RMSE) on the precipitation field for the first 24 hours for both EnKF and 3DVar simulations.
715 In general, the EnKF provides the lowest (best) RMSE scores, with respect to 3DVar. Also,
716 note that the impact of the assimilation of reflectivity observations does not last more than 4-6
717 hours, in accordance with past studies.

718 8.1.2. ROC and AUC

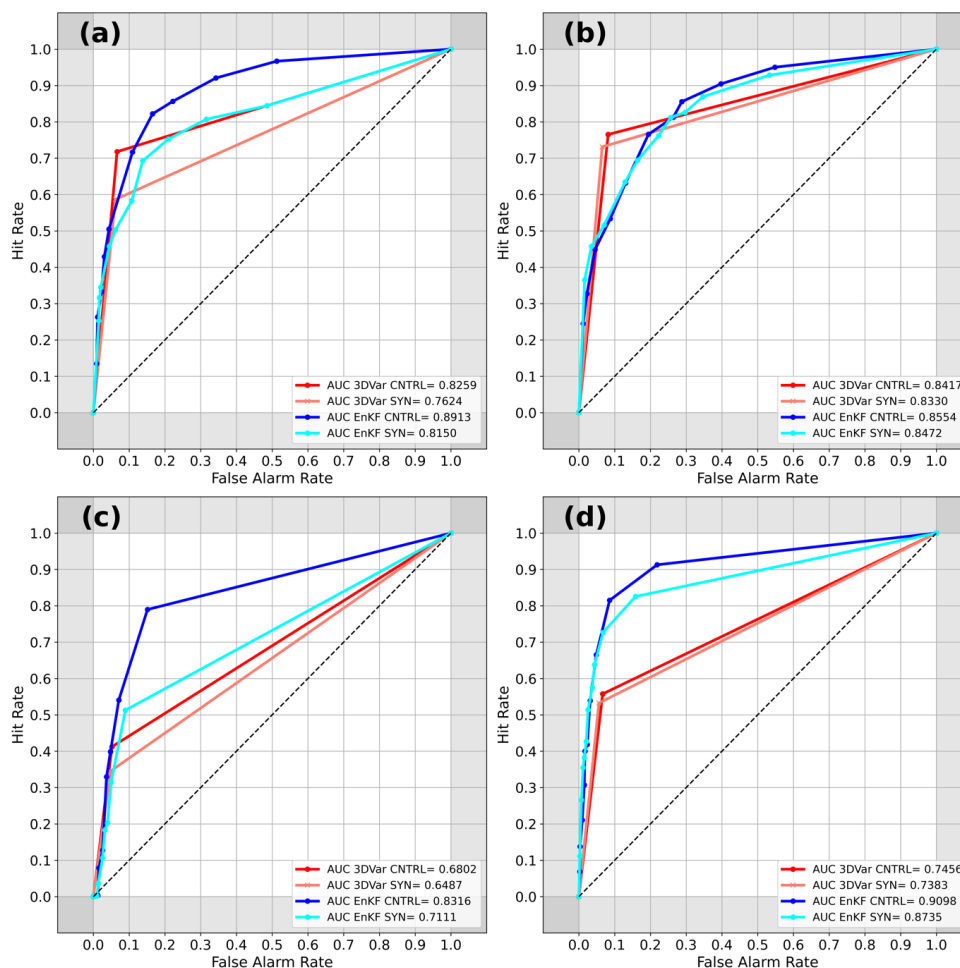
719 To strengthen how skillful are the different simulations performed by the 3DVar and the EnKF,
720 the *Receiver Operating Characteristic* (ROC) curve is used. The probability of exceeding a
721 given threshold is computed and verified against dichotomous observations. The ROC curve is
722 computed as follows: the model variable is interpolated to the observation locations and if the
723 model variable exceeds a given threshold, that model grid point is assigned a value of 1. On
724 the contrary, if the model value does not exceed that threshold, the assigned value is 0. The
725 same method is applied for the observations. Then, using these dichotomous values, the Hit
726 Rate and False Alarm scores are computed. This process is repeated, varying the threshold
727 value. Gathering the Hit Rate and False Alarm scores for the different thresholds, we obtain
728 the ROC curve. For the 3DVar, we get the Hit Rate and False Alarm scores by simply
729 interpolating the model values to the observation locations and apply the threshold criteria
730 explained above. In the case of the EnKF, the ensemble mean is used as the field to be
731 interpolated to the observation locations. The area under the ROC curve (AUC), which
732 measures the ability of the system to discriminate between the occurrence or nonoccurrence of
733 the event, is also computed.

734 For the sake of brevity and because the results from the three sub-regions are similar, the ROC
735 and the area under the ROC curve are computed, accounting for all the observations within the



736 inner numerical domain. Specifically, to compute the ROC curves, we use the 3-hour (from 00
737 UTC - 03 UTC 15 Oct) and 6-hour (from 00 UTC - 06 UTC 15 Oct) accumulated precipitation
738 fields from the numerical model and the observed values registered by the rain gauges, using 1
739 mm and 10 mm as thresholds (Fig. 9).

740 Results show that EnKF clearly outperforms 3DVar for the different accumulated precipitation
741 rates and thresholds, depicting larger values of AUCs. An even bigger improvement is obtained
742 using a larger threshold (i.e., bottom row of Fig. 9) for EnKF, where the benefits of assimilating
743 radar observations are noticeable, in comparison with 3DVar. To better understand this result,
744 we inspected in more detail the 1-h and 6-h accumulated precipitation fields obtained from the
745 EnKF (CNTRL) and the 3DVar (CNTRL) and we compared those fields against the
746 corresponding observations (see Fig. A1 in the Appendix). The 1-h accumulated precipitation
747 (first row, Fig. A1) shows that the EnKF is localizing with high accuracy the regions where the
748 most intense precipitation was observed, that is near Tuscany and northern Italy. Also, 3DVar
749 correctly reproduces the rainfall in the regions affected by observed precipitation, although the
750 maximum amounts are centered over Liguria, instead of near Tuscany. In addition, the 3DVar
751 is also showing a tongue area of weak precipitation from Liguria to northern Italy, that does
752 not fit with the observations. Hence, although there are some differences between 3DVar and
753 EnKF for the 1-h accumulated precipitation field, because the accumulated precipitation values
754 are small, the ROC verification scores from the EnKF and 3DVar do not differ significantly.
755 However, in the case of the 6-h accumulated precipitation (second row, Fig. A1), the 3DVar
756 produces higher values of accumulated precipitation near Liguria, Tuscany and northern Italy
757 than the observed ones. Moreover, 3DVar is also misplacing the locations of the precipitation
758 for some places. On the contrary, the EnKF can (a) locate with enough accuracy the regions
759 where the accumulated precipitation was actually observed, (b) properly estimate the observed
760 intensity and (c) avoid spatial errors associated with the location where the precipitation was
761 produced. This is why ROC for the 6-hour accumulated precipitation obtained from the EnKF
762 produced a much better score than the 3DVar. We hypothesize that this difference could be
763 associated with the *static/climatological* background error covariance matrix used by the
764 3DVar. Because of the fast changes in the flow associated with the IOP13 case, using a
765 climatological background error covariance could not be as good as using a flow-dependent
766 background error covariance matrix, which is used in the EnKF.



767
 768 Figure 9. ROC curves and AUC associated with the 3DVar (red colors) and EnKF (blue colors) for the 3-hour
 769 accumulated precipitation using (a) 1 mm and (b) 10 mm threshold and 6-hour accumulated precipitation using
 770 (c) 1 mm and (d) 10 mm threshold, computed over the entire inner domain.

771

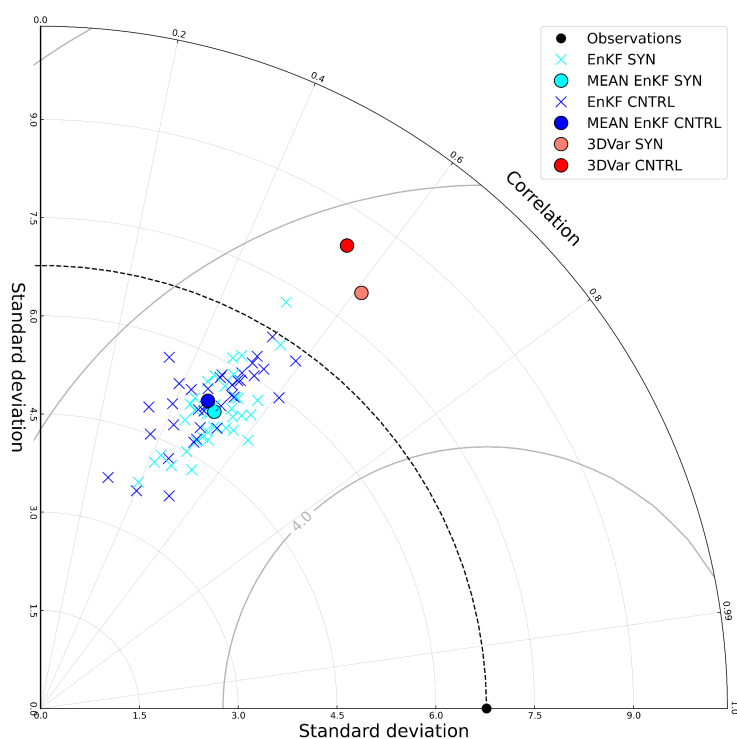
772 8.1.3. Taylor Diagrams

773 To strengthen the comparison of the DA schemes, the Taylor Diagram is used. This tool
 774 provides us with extra information about the skill of each ensemble member in the case of the
 775 EnKF. Here, we compute the Taylor diagram over the 6-hour accumulated precipitation field,
 776 which is the range where the observations assimilated have more impact on the forecast.
 777 Results show that the 3DVar and the ensemble mean of the EnKF provide similar results, with
 778 similar correlations (0.50-0.61), similar root mean squared error and standard deviation that are
 779 distributed symmetrically about the observation value, with the 3DVar overestimating the
 780 standard deviation and the EnKF underestimating it (Fig. 10). However, if we consider each
 781 ensemble member, we can observe that there is a cluster of the ensemble members of the EnKF
 782 that provide better scores than the 3DVar. Although the difference between the EnKF and the
 783 3DVar in this case is small, we can point out that the EnKF provides additional information



784 from their individual ensemble members. For instance, the individual ensemble members
785 showing higher correlation and standard deviation similar to the observations for this study are
786 the ones using Grell-Freitas cumulus parameterization in combination with the Yonsei
787 University planetary boundary layer scheme. Ensemble members associated with the lower
788 scores are those using Kain-Fritsch for the cumulus parameterization and the Mellor-Yamada-
789 Janjic for the planetary boundary layer scheme.

790



791

792 Figure 10. Taylor diagram performed by the 3DVar (reds) and EnKF (blues) for the 6-hour accumulated
793 precipitation valid at 06 UTC 15 October 2012.

794

795 8.2. Statistical analysis: Qendresa event

796 Typically, two key factors are investigated for Tropical cyclone forecasts: (a) the intensity and
797 (b) the trajectory followed by the cyclone. Therefore, to assess the impact of assimilating both
798 *in-situ* conventional and remote RSAMV observations using the 3DVar and the EnKF, these
799 two factors are considered.

800

801

802

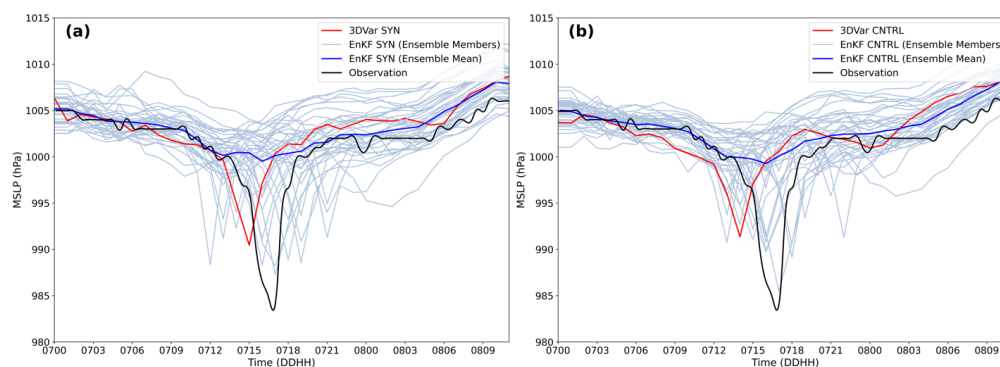
803



804 8.2.1. Whisker Diagrams

805 For this event, the lack of *in-situ* observations over maritime regions poses a main challenge to
806 properly verify the triggering and intensification of cyclones. Fortunately, the Qendresa
807 medicane crossed just over Malta island, where a pressure drop greater than 20 hPa in 6 h, was
808 registered by METARs at Malta airport, reaching a minimum of surface pressure of 985 hPa.
809 Therefore, this METAR is used to quantitatively assess the skill of the different DA
810 simulations. To compare the surface pressure registered at Malta with the different simulations,
811 the full cyclone trajectory is used, and the grid point closest to Malta airport is selected. Finally,
812 the surface pressure time series associated with that model grid point is compared with the
813 values registered at Malta airport. Specifically, the surface pressure time series measured by
814 METAR is compared with the different DA simulations from 3DVar and EnKF, such as the
815 3DVar_SYN, 3DVar_CNTRL, EnKF_SYN, and the EnKF_CNTRL (Fig. 11).

816



817
818 Figure 11. Temporal surface pressure evolution at the closes grid point to Malta for the (a) SYN and (b) CNTRL
819 experiments associated with the EnKF (blue lines) and 3DVar (red lines), compared to the observed surface
820 pressure registered by METARs in Malta's airport.

821

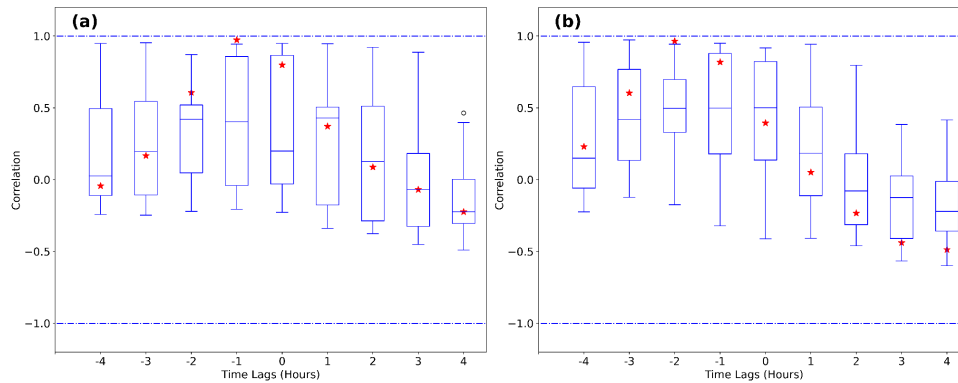
822 Results from the assimilation of *in-situ* conventional observations show that the ensemble mean
823 of the EnKF_SYN accurately fits the observations during the first hours of the forecast, from
824 00 UTC to 13 UTC 7 November (Fig. 11a), performing slightly better than 3DVAR_SYN.
825 However, during the intensification phase, the ensemble mean of the EnKF_SYN barely shows
826 the intensification of Qendresa, reaching minimum MSLP values of 1002 hPa. On the contrary,
827 the 3DVar_SYN simulation depicts the intensification of the medicane, by deepening the
828 MSLP and reaching values of 992 hPa, although a time shift of 3 hours is found (i.e., 15 UTC
829 7 November) (Fig. 11a). Finally, during the dissipation phase of Qendresa, the ensemble mean
830 of EnKF_SYN is performing a bit better than the 3DVar_SYN (Fig. 11a). This interesting
831 result clearly shows a limitation of the EnKF when applied to low-predictable weather events,
832 such as Qendresa. The low predictability and the high sensitivity to the different physical
833 parameterization schemes used for the forecast of this kind of event, lead to a very different
834 behavior of each ensemble member. Consequently, some members could completely fail in the
835 prediction of the weather event. In this situation, our small-to-moderate ensemble will probably
836 produce a poor flow-dependent background error covariance matrix, which is key in DA,
837 resulting in an analysis ensemble with large spread, for which ensemble mean will be smoothed
838 out significantly. On the other hand, in such situations, we could think of using a
839 climatological/static background error covariance matrix, as the one used in the 3DVar. If this



840 climatological background error covariance matrix is obtained with a large enough statistical
841 sample, it could produce much better results than using the flow-dependent background error
842 covariance computed with ensemble members that are not accurate enough, as we see in Fig.
843 11a when we compared the 3DVar (red line) with the EnKF ensemble mean analysis (blue
844 line). Also, it is important to note that although the ensemble mean of the EnKF_SYN is not
845 correctly reproducing the intensification of Qendresa, some of the ensemble members
846 accurately reproduce the observed MSLP both in deepening and timing. This suggests that
847 using an ensemble system, even having the above-mentioned problems, is still more useful than
848 using only a fully deterministic system such as the 3DVar, which cannot provide information
849 about the uncertainties of the system. Therefore, we can speculate that for extreme weather
850 events with low numerical predictability, a better approach could be using a Hybrid error
851 covariance model, where the forecast error covariance matrix is obtained linearly combining
852 ensemble-based covariance with static climatological error covariances (Hamill and Snyder
853 (2000); Lorenc (2003); Clayton et al., 2013; Carrió et al., 2021). The impact of using hybrid
854 DA to improve this kind of small-scale extreme weather events could be of great interest in the
855 weather forecast community, although it is beyond the scope of this study. For this reason, the
856 authors leave as future work the benefits of using hybrid error covariance models to improve
857 the forecast of extreme weather events in the Mediterranean basin.

858 Then, we evaluated the impact of assimilating both *in-situ* conventional and RSAMV
859 observations in the improvement of Qendresa intensity forecast. In this case, the results show
860 large similarities with the assimilation of only *in-situ* observations (Fig. 11b). In terms of the
861 3DVar, the MSLP signature is basically the same, without showing a clear signal of
862 improvement or diminishing, suggesting that the assimilation of RSAMVs is not enough to
863 significantly improve the low level relevant dynamical structures associated with the genesis
864 and intensification of Qendresa. However, in terms of the EnKF a clear improvement for a few
865 members is found, even if it is not affecting the mean value. Indeed, some of the ensemble
866 members depicting an intense cyclone far from the time when it was observed (approx. at 18
867 UTC 7 November), were corrected reducing spurious cyclones and the deepening of at least
868 one ensemble member close to the observed value (Fig. 11b). It can be observed that in the
869 EnKF_CNTRL, there are more ensemble members depicting a deep cyclone at the observed
870 time than in the case of the EnKF_SYN, showing the benefits of assimilating RSAMVs to
871 improve the intensification estimation of Qendresa.

872 To quantitatively assess the performance of the different DA experiments, we use the *lagged*
873 *correlation* technique computed between the model MSLP signatures and the observations.
874 This technique allows us to measure how the shape of the surface pressure evolution obtained
875 from the different simulations fits the shape of the observed MSLP, taking also into account
876 temporal shifting. The correlation is computed for the deterministic 3DVar, and for each
877 ensemble member from the EnKF. These results are shown using Whisker plots (Fig. 12).
878 Notice that a correlation of one means that the specific model field has the same ‘V’ pressure
879 shape evolution as the observation, and that the minimum for both is found at the same time.
880 For the 3DVar_SYN, the correlation is maximum and approximately equal to one when 1-hour
881 delay is applied to forecasts (Fig. 12a). Whiskers from EnKF_SYN show that none of the
882 ensemble members overcomes the maximum correlation value found in 3DVar_SYN.
883 However, when the assimilation of RSAMVs is added to the *in-situ* conventional observations,
884 it is found that the maximum correlation value associated with 3DVar_CNTRL using 2h of
885 delay applied to the forecasts, is surpassed by some of the ensemble members of the
886 EnKF_CNTRL, when a 3 or 4 hour of delay is applied (Fig. 12b).



887
888 Figure 12. Whisker plots depicting the lagged correlation values between the observations and the EnKF (blue
889 boxes) and the 3DVar (red stars) for the (a) SYN and (b) CNTRL experiments. The correlation is computed
890 considering that the observed V-shape pressure signature associated with the observations is shifted 4 hours to the
891 left and 4 hours to the right.

892

893 8.2.2. Probability Distribution of Cyclone Center Occurrence

894 Due to the difficulty to accurately predict the observed trajectory of Qendresa (Pytharoulis et
895 al., 2018), the impact of assimilating different kinds of observations on the trajectory of the
896 medicane is investigated.

897 The 3DVar_SYN is capturing with enough accuracy the track of Qendresa during the first
898 hours (Fig. 13b). However, for 3DVar_SYN the trajectory of Qendresa leaving Malta diverges
899 from the observed trajectory, moving north-eastwards without showing the track-loop signal
900 observed by satellite imagery. To quantify the benefits of assimilating *in-situ* conventional
901 observations using the 3DVar or the EnKF, the probability of occurrence of a cyclone following
902 the track observed via satellite imagery is computed. For instance, we can see that the
903 probability of cyclone occurrence eastwards Sicily, where Qendresa made landfall while it was
904 doing a loop, is too small according to 3DVar_SYN (Fig. 13b). On the other hand, some of the
905 ensemble members depict a cyclone trajectory for EnKF_SYN that is largely shifted
906 southward, whereas some of them reproduce the loop trajectory that deterministic numerical
907 weather models miss performing (Fig. 13a). In addition, the probability of Qendresa occurrence
908 eastwards Sicily, is in this case larger than for 3DVar_SYN, showing the benefits of using the
909 EnKF against the 3DVar (Fig. 13a). Moreover, the EnKF_SYN ensemble trajectories, in
910 general, follow a ‘V’ shape (i.e., first moving towards the southeast, then moving to the east
911 and finally moving towards the northeast) similar to the trajectory observed via satellite
912 imagery. Although the shape of most of the EnKF_SYN trajectories agree with the
913 observations, the location is not accurate, showing a general shift towards the southeast.

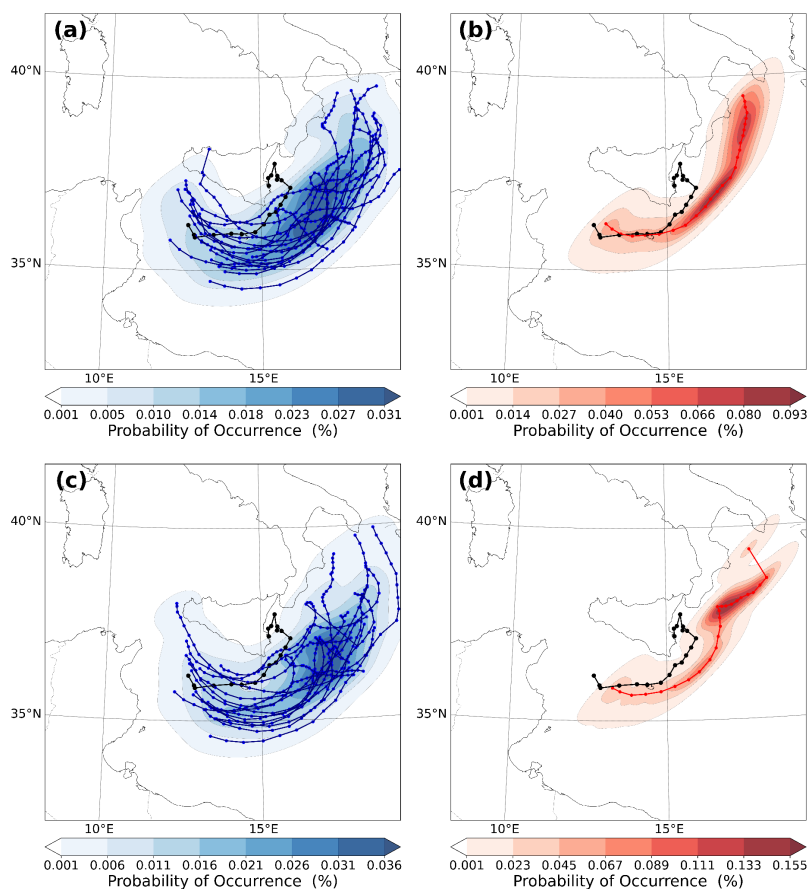
914 If both *in-situ* conventional and RSAMV observations are assimilated, some of the ensemble
915 members from the EnKF_CNTRL shows more accurate trajectories in comparison with
916 EnKF_SYN: the loop trajectory is close to the observed region of eastern Sicily (Fig. 13c). An
917 improvement of the 3DVar_CNTRL trajectory by increasing the probability of cyclone
918 occurrence following the observed track is observed, especially eastern of Sicily. However,
919 3DVar experiments are not able to reproduce the looping trajectory observed via satellite
920 imagery (Fig. 13b-d). Hence, EnKF outperforms 3DVar showing some of the ensemble



921 members depicting a loop trajectory, although shifted southwards and producing a probability
922 of cyclone occurrence smaller than the 3DVAR ones.

923 Both the EnKF and the 3DVar still have difficulties in depicting accurately the track observed
924 by Qendresa, even after the assimilation of *in-situ* conventional and RSAMV observations.
925 Because RSAMVs are more useful in describing dynamical features on the upper levels of the
926 atmosphere, we hypothesize that ingesting them via DA may not be enough to correct key low-
927 level dynamical features. In this case, the assimilation of surface wind observations may help
928 to even improve these results. However, this is beyond the scope of this study and the authors
929 leave this question as future work, where other sources of information from satellites will be
930 assimilated to improve low-level thermodynamic aspects of extreme weather events, such as
931 medicanes.

932



933

934 Figure 13. Probability of cyclone center occurrence computed using Gaussian KDE for (a) EnKF (SYN), (b)
935 3DVar (SYN), (c) EnKF (CNTRL) and (d) 3DVar (CNTRL), from 11 UTC 7 November to 12 UTC 8 November
936 2014. Qendresa's trajectory observed via satellite imagery is depicted in black.

937

938



939 9. Summary and Conclusions

940 In this study, we quantitatively assess the impact of two high-resolution DA techniques. Here,
941 we focus on the impact of assimilating observations to improve warning lead times of extreme
942 weather events. While previous studies often assimilate observations during the mature stage
943 of a weather event, when it is fully developed and no time for action remains, here the
944 observations are assimilated hours before the mature stage of the convective system is reached,
945 during the pre-convective stage. This approach enhances the accuracy of the pre-convective
946 environment, thereby increasing the time available for reaction and preparedness. To
947 quantitatively evaluate their forecast skill in improving the predictability of maritime events,
948 two extreme weather events triggered over the sea affecting populated coastal regions are used.
949 Nowadays, these weather events represent a serious challenge for the numerical weather
950 prediction community in terms of their accurate predictability, due to their initialization over
951 the sea, which are regions with a lack of in-situ observations, and thus their initial conditions
952 are poorly estimated. Furthermore, these convective systems evolved towards complex terrain
953 regions, increasing the predictability challenges. These two extreme weather events are known
954 as (a) the high precipitation event registered during the 13th Intensive Observation Period
955 (IOP13) affecting the western, northern and central parts of Italy, and (b) the intense Tropical-
956 like Mediterranean Cyclone (medicane) known as Qendresa, that affected the islands of
957 Pantelleria, Lampedusa, Malta and Sicily.

958 The two DA methods compared in this study for IOP13 and Qendresa are the variational 3DVar
959 and the ensemble-based EnKF, which are currently used in operational National Weather
960 Services worldwide. For the two events, both DA methods are used, and the type and number
961 of assimilated observations changes depending on the data availability. For Qendresa, we
962 assimilated (a) hourly *in-situ* conventional observations and (b) wind speed and wind direction
963 profiles of the entire atmosphere (RSAMVs) derived from geostationary satellites every 20-
964 min, providing high spatial and temporal resolution observations covering the Central
965 Mediterranean Sea, where Qendresa initiated and evolved. On the other hand, for the IOP13,
966 we assimilated (a) hourly *in-situ* conventional observations and (b) 15-min 3D reflectivity
967 observations from two type-C Doppler Weather Radars.

968 Because of the different thermodynamic characteristics associated with Qendresa and IOP13,
969 a set of different verification metrics were used for each of these extreme weather events. The
970 *Filtering method* (FSS and RMSE), the ROC/AUC and the *Taylor diagram* were used to verify
971 the numerical simulations from 3DVar and EnKF associated with IOP13. In the case of
972 Qendresa, we used the *Whisker diagrams* and the *Probability Distribution of Cyclone Center*
973 *Occurrence* verification scores. For the IOP13 event, the *Filtering method* and the *Taylor*
974 *diagram* verification scores indicate that the skill performance of the 3DVar and the EnKF is
975 similar, although the EnKF slightly overcomes the 3DVar. In addition, it was observed that the
976 assimilation of spatial and temporal high-resolution reflectivity observations significantly
977 improved the forecast for both 3DVar and EnKF, showing the key role of this type of
978 observation. On the other hand, the ROC and AUC scores clearly show that EnKF outperforms
979 3DVar. For the Qendresa event, although the ensemble mean of EnKF provides the worst
980 results, in terms of the intensity of the medicane with respect to 3DVar, some of the EnKF
981 ensemble members provide better results than 3DVar. This result suggests how important it is
982 using an ensemble forecast system to predict extreme weather events at high spatial and
983 temporal resolution. In terms of the trajectory of the cyclone, it is also shown that using the
984 EnKF provides a more realistic insight of the real trajectory Qendresa followed.



985 Although the EnKF technique has shown in general better performance against the 3DVar for
986 the two extreme weather events analyzed in this study, it is also important to account for the
987 computational resources required to use them. In this sense, the 3DVar requires much less
988 computational resources than the EnKF because it does not need to build an ensemble of
989 considerable size, and it does not need either to simulate model trajectories between the
990 assimilation of a set of observations at time t_1 and the subsequent set of observations valid at
991 t_2 . This makes the 3DVar appealing because it is much faster and cheaper than the EnKF, and
992 it makes this technique particularly suitable for operational purposes at the small weather
993 forecast centers.

994 Another interesting result that we have shown in this study is that depending on the level of
995 predictability of the weather event and its sensitivity to numerical physical parameterizations
996 used to build our ensemble, the 3DVar performs better than the EnKF ensemble mean. We
997 speculated that this is linked to the way the background error covariances from these two
998 methods are built. Based on this, we suppose that a better approach could be using Hybrid error
999 covariance models, where the forecast error covariance matrix is obtained linearly combining
1000 the ensemble-based error covariance from the EnKF and the static climatological error
1001 covariance matrix from the 3DVar. Further work will investigate the impact of using hybrid
1002 DA schemes in comparison to use standard 3DVar or EnKF. As a case study, a catastrophic
1003 and deadly flash flood event affecting the Balearic Islands will be used to quantitatively assess
1004 the skill performance of the hybrid DA scheme against the EnKF and a more advanced version
1005 of the 3DVar, which is known as the 4DVar. In this case, most of the ensemble members of the
1006 EnKF did not reproduce the convective cells that later resulted in the flash flood episode. This
1007 is a key problem in current ensemble-based DA research. In this scenario, it is expected that
1008 the hybrid error covariance matrix will be more precise than the one derived from the ensemble
1009 members or from climatology, which on their own are not properly reproducing key aspects of
1010 this extreme weather episode. High temporal and spatial observations from Doppler Weather
1011 radars, such as reflectivity and radial wind velocities, will be assimilated for this case to obtain
1012 accurate analysis and thus, improve the short-range forecast of this catastrophic flash-flood
1013 event.

1014

1015 **Acknowledgements:**

1016

1017 The first author acknowledges the *Ministerio de Universidades (Plan de Recuperación,*
1018 *Transformación y Resiliencia)* funded by the European Union (NextGenerationEU), with the
1019 participation of the University of the Balearic Islands, which supports his current postdoctoral
1020 position as a *Maria Zambrano* Fellowship. However, it should be noted that the viewpoints
1021 and opinions expressed in the relevant cases, or resulting from the grant, are the sole
1022 responsibility of the author or authors and do not necessarily represent the views of the
1023 European Union or the European Commission. Neither the European Union nor the European
1024 Commission can be held liable for any of the opinions expressed. This research is also
1025 sponsored by the Ministerio de Ciencia e Innovación-Agencia Estatal de Investigación
1026 TRAMPAS (PID2020-113036RB-I00/AEI/10.13039/501100011033). The authors thankfully
1027 acknowledge Météo-France for supplying the data and HyMeX database teams (ESPRI/IPSL
1028 and SEDOO/OMP) for their help in accessing the data. The author also acknowledges the
1029 computer resources at MareNostrum IV and CRAY supercomputers, as well as the technical
1030 support provided by the Barcelona Supercomputer Center (RES-AECT-2017-1-0014, RES-



1031 AECT-2017-2-0014) and ECMWF data center, required to perform the high-resolution
1032 simulations presented in this study.

1033

1034

1035

1036

1037

1038 **References**

1039

1040 Albergel, C., Zheng, Y., Bonan, B., Dutra, E., Rodríguez-Fernández, N., Munier, S., ... & Calvet, J. C.
1041 (2020). Data assimilation for continuous global assessment of severe conditions over terrestrial
1042 surfaces. *Hydrology and Earth System Sciences*, 24(9), 4291-4316.

1043

1044 Amengual, A., Carrió, D. S., Ravazzani, G., & Homar, V. (2017). A comparison of ensemble
1045 strategies for flash flood forecasting: The 12 october 2007 case study in Valencia, Spain. *Journal of*
1046 *Hydrometeorology*, 18(4), 1143-1166.

1047

1048 Amengual, A., Hermoso, A., Carrió, D. S., & Homar, V. (2021). The Sequence of Heavy Precipitation
1049 and Flash Flooding of 12 and 13 September 2019 in Eastern Spain. Part II: A Hydrometeorological
1050 Predictability Analysis Based on Convection-Permitting Ensemble Strategies. *Journal of*
1051 *Hydrometeorology*, 22(8), 2153-2177.

1052

1053 Anderson, J. L., & Anderson, S. L. (1999). A Monte Carlo implementation of the nonlinear filtering
1054 problem to produce ensemble assimilations and forecasts. *Monthly weather review*, 127(12), 2741-
1055 2758.

1056

1057 Anderson, J. L. (2001). An ensemble adjustment Kalman filter for data assimilation. *Monthly weather*
1058 *review*, 129(12), 2884-2903.

1059

1060 Anderson, J. L., & Collins, N. (2007). Scalable implementations of ensemble filter algorithms for data
1061 assimilation. *Journal of Atmospheric and Oceanic Technology*, 24(8), 1452-1463.

1062

1063 Anderson, J., Hoar, T., Raeder, K., Liu, H., Collins, N., Torn, R., & Avellano, A. (2009). The data
1064 assimilation research testbed: A community facility. *Bulletin of the American Meteorological Society*,
1065 90(9), 1283-1296.

1066

1067 Barker DM, Huang W, Guo Y-R, Bourgeois A, Xiao XN (2004) A three-dimensional variational data
1068 assimilation system for MM5: implementation and initial results. *Mon Wea Rev* 132:897–914

1069

1070 Bowman, A. W., & Azzalini, A. (1997). *Applied smoothing techniques for data analysis: the kernel*
1071 *approach with S-Plus illustrations* (Vol. 18). OUP Oxford.

1072

1073 Bryan, G. H., & Rotunno, R. (2005, October). Statistical convergence in simulated moist absolutely
1074 unstable layers. In *Preprints, 11th Conf. on Mesoscale Processes*, Albuquerque, NM, Amer. Meteor.
1075 Soc. M (Vol. 1).

1076



- 1077 Carrassi, A., Bocquet, M., Bertino, L., & Evensen, G. (2018). Data assimilation in the geosciences: An
1078 overview of methods, issues, and perspectives. *Wiley Interdisciplinary Reviews: Climate Change*, 9(5),
1079 e535.
- 1080
- 1081 Carrió, D. S., & Homar, V. (2016). Potential of sequential EnKF for the short-range prediction of a
1082 maritime severe weather event. *Atmospheric Research*, 178, 426-444.
- 1083
- 1084 Carrió, D. S., Homar, V., Jansa, A., Romero, R., & Picornell, M. A. (2017). Tropicalization process of
1085 the 7 November 2014 Mediterranean cyclone: Numerical sensitivity study. *Atmospheric Research*, 197,
1086 300-312.
- 1087
- 1088 Carrió, D. S., Homar, V., & Wheatley, D. M. (2019). Potential of an EnKF storm-scale data assimilation
1089 system over sparse observation regions with complex orography. *Atmospheric Research*, 216, 186-206.
- 1090
- 1091 Carrió, D. S., Bishop, C. H., & Kotsuki, S. (2021). Empirical determination of the covariance of forecast
1092 errors: An empirical justification and reformulation of hybrid covariance models. *Quarterly Journal of*
1093 *the Royal Meteorological Society*, 147(736), 2033-2052.
- 1094
- 1095 Carrió, D. S. (2023): Improving the predictability of the Qendresa Medicane by the assimilation of
1096 conventional and atmospheric motion vector observations. Storm-scale analysis and short-range
1097 forecast, *Nat. Hazards Earth Syst. Sci. Discuss.* <https://doi.org/10.5194/nhess-2022-58>,
- 1098
- 1099 Cioni, G, Cerrai, D, Klocke, D. (2018). Investigating the predictability of a Mediterranean tropical-like
1100 cyclone using a storm-resolving model. *Q J R Meteorol Soc.*; 144: 1598– 1610.
1101 <https://doi.org/10.1002/qj.3322>
- 1102
- 1103 Clayton, A. M., Lorenc, A. C., & Barker, D. M. (2013). Operational implementation of a hybrid
1104 ensemble/4D-Var global data assimilation system at the Met Office. *Quarterly Journal of the Royal*
1105 *Meteorological Society*, 139(675), 1445-1461.
- 1106
- 1107 Courtier, P. H. I. L. I. P. P. E., Thépaut, J. N., & Hollingsworth, A. (1994). A strategy for operational
1108 implementation of 4D-Var, using an incremental approach. *Quarterly Journal of the Royal*
1109 *Meteorological Society*, 120(519), 1367-1387.
- 1110
- 1111 Di Muzio, E, Riemer, M, Fink, AH, Maier-Gerber, M. Assessing the predictability of Medicanes in
1112 ECMWF ensemble forecasts using an object-based approach. *Q J R Meteorol Soc.* 2019; 145: 1202–
1113 1217. <https://doi.org/10.1002/qj.3489>
- 1114
- 1115 Drobinski, P., Ducrocq, V., Alpert, P., Anagnostou, E., Béranger, K., Borga, M., ... & Wernli, H. (2014).
1116 HyMeX: A 10-year multidisciplinary program on the Mediterranean water cycle. *Bulletin of the*
1117 *American Meteorological Society*, 95(7), 1063-1082.
- 1118
- 1119 Dudhia, J. (1989). Numerical study of convection observed during the winter monsoon experiment
1120 using a mesoscale two-dimensional model. *Journal of Atmospheric Sciences*, 46(20), 3077-3107.
- 1121
- 1122 Eliassen, A. (1954). Provisional report on calculation of spatial covariance and autocorrelation of the
1123 pressure field. Peport no 5, Videnskaps-Akademiets Institutt for Vaer-Og Klimaforskning, Oslo,
1124 Norway, 12.



- 1125
1126 Emanuel, K. (2005). Genesis and maintenance of "Mediterranean hurricanes". *Advances in*
1127 *Geosciences*, 2, 217-220.
1128
1129 Evensen, G. (1994). Sequential data assimilation with a nonlinear quasi-geostrophic model using Monte
1130 Carlo methods to forecast error statistics. *Journal of Geophysical Research: Oceans*, 99(C5), 10143-
1131 10162.
1132
1133 Ferrer Hernández, A. L., González Jardines, P. M., Sierra Lorenzo, M., & de la Caridad Aguiar
1134 Figueroa, D. (2022). Impact of the Assimilation of Non-Precipitating Echoes Reflectivity Data on the
1135 Short-Term Numerical Forecast of SisPI. *Environmental Sciences Proceedings*, 19(1), 13.
1136
1137 Ferretti, R., Pichelli, E., Gentile, S., Maiello, I., Cimini, D., Davolio, S., ... & Rotunno, R. (2014).
1138 Overview of the first HyMeX Special Observation Period over Italy: observations and model results.
1139 *Hydrology and Earth System Sciences*, 18(5), 1953-1977.
1140
1141 Flaounas, E., Lagouvardos, K., Kotroni, V., Claud, C., Delanoë, J., Flamant, C., ... & Wernli, H. (2016).
1142 Processes leading to heavy precipitation associated with two Mediterranean cyclones observed during
1143 the HyMeX SOP1. *Quarterly Journal of the Royal Meteorological Society*, 142, 275-286.
1144
1145 Garcies, L., & Homar, V. (2009). Ensemble sensitivities of the real atmosphere: application to
1146 Mediterranean intense cyclones. *Tellus A: Dynamic Meteorology and Oceanography*, 61(3), 394-406.
1147
1148 Gaspari, G., & Cohn, S. E. (1999). Construction of correlation functions in two and three dimensions.
1149 *Quarterly Journal of the Royal Meteorological Society*, 125(554), 723-757.
1150
1151 Grell, G. A., & Freitas, S. R. (2014). A scale and aerosol aware stochastic convective parameterization
1152 for weather and air quality modeling. *Atmospheric Chemistry and Physics*, 14(10), 5233-5250.
1153
1154 Hacker, J. P., Anderson, J. L., & Pagowski, M. (2007). Improved vertical covariance estimates for
1155 ensemble-filter assimilation of near-surface observations. *Monthly Weather Review*, 135(3), 1021-
1156 1036.
1157
1158 Hamill, T. M., & Snyder, C. (2000). A hybrid ensemble Kalman filter–3D variational analysis scheme.
1159 *Monthly Weather Review*, 128(8), 2905-2919.
1160
1161 Honda, T., Miyoshi, T., Lien, G. Y., Nishizawa, S., Yoshida, R., Adachi, S. A., ... & Bessho, K. (2018).
1162 Assimilating all-sky Himawari-8 satellite infrared radiances: A case of Typhoon Soudelor (2015).
1163 *Monthly Weather Review*, 146(1), 213-229.
1164
1165 Hong, S. Y., Noh, Y., & Dudhia, J. (2006). A new vertical diffusion package with an explicit treatment
1166 of entrainment processes. *Monthly weather review*, 134(9), 2318-2341.
1167
1168 Houtekamer, P. L., & Mitchell, H. L. (1998). Data assimilation using an ensemble Kalman filter
1169 technique. *Monthly Weather Review*, 126(3), 796-811.
1170



- 1171 Huang, X. Y., Xiao, Q., Barker, D. M., Zhang, X., Michalakes, J., Huang, W., ... & Kuo, Y. H. (2009).
1172 Four-dimensional variational data assimilation for WRF: Formulation and preliminary results. *Monthly*
1173 *Weather Review*, 137(1), 299-314.
1174
1175 Iacono, M. J., Delamere, J. S., Mlawer, E. J., Shephard, M. W., Clough, S. A., & Collins, W. D. (2008).
1176 Radiative forcing by long-lived greenhouse gases: Calculations with the AER radiative transfer models.
1177 *Journal of Geophysical Research: Atmospheres*, 113(D13).
1178
1179 Janjić, Z. I. (1990). The step-mountain coordinate: Physical package. *Monthly weather review*, 118(7),
1180 1429-1443.
1181
1182 Janić, Z. I. (2001). Nonsingular implementation of the Mellor-Yamada level 2.5 scheme in the NCEP
1183 Meso model.
1184
1185 Jansa, A., Alpert, P., Arbogast, P., Buzzi, A., Ivancan-Picek, B., Kotroni, V., ... & Speranza, A. (2014).
1186 MEDEX: a general overview. *Natural Hazards and Earth System Sciences*, 14(8), 1965-1984.
1187
1188 Kain, J. S., & Fritsch, J. M. (1990). A one-dimensional entraining/detraining plume model and its
1189 application in convective parameterization. *Journal of Atmospheric Sciences*, 47(23), 2784-2802.
1190
1191 Kain, J. S. (2004). The Kain–Fritsch convective parameterization: an update. *Journal of applied*
1192 *meteorology*, 43(1), 170-181.
1193
1194 Kalnay, E. (2003). *Atmospheric modeling, data assimilation and predictability*. Cambridge university
1195 press.
1196
1197 Le Dimet, F. X., & Talagrand, O. (1986). Variational algorithms for analysis and assimilation of
1198 meteorological observations: theoretical aspects. *Tellus A: Dynamic Meteorology and Oceanography*,
1199 38(2), 97-110.
1200
1201 Lee, J. H., Lee, H. H., Choi, Y., Kim, H. W., & Lee, D. K. (2010). Radar data assimilation for the
1202 simulation of mesoscale convective systems. *Advances in Atmospheric Sciences*, 27, 1025-1042.
1203
1204 Li, X., J. Ming, M. Xue, Y. Wang, and K. Zhao, 2015: Implementation of a dynamic equation constraint
1205 based on the steady state momentum equations within the WRF hybrid ensemble-3DVar data
1206 assimilation system and test with radar T-TREC wind assimilation for tropical Cyclone Chanthu (2010).
1207 *J. Geophys. Res. Atmos.*, 120, 4017–4039, doi: 10.1002/2014JD022706.
1208
1209 Li, X., Zeng, M., Wang, Y., Wang, W., Wu, H., & Mei, H. (2016). Evaluation of two momentum control
1210 variable schemes and their impact on the variational assimilation of radarwind data: Case study of a
1211 squall line. *Advances in Atmospheric Sciences*, 33, 1143-1157.
1212
1213 Lorenc, A. C. (1981). A global three-dimensional multivariate statistical interpolation scheme. *Monthly*
1214 *Weather Review*, 109(4), 701-721.
1215
1216 Lorenc, A. C. (1986). Analysis methods for numerical weather prediction. *Quarterly Journal of the*
1217 *Royal Meteorological Society*, 112(474), 1177-1194.
1218



- 1219 Lorenc, A. C. (2003). The potential of the ensemble Kalman filter for NWP—A comparison with 4D-
1220 Var. Quarterly Journal of the Royal Meteorological Society: A journal of the atmospheric sciences,
1221 applied meteorology and physical oceanography, 129(595), 3183-3203.
1222
- 1223 Llasat, M., & Sempere-Torres, D. (2001). Heavy rains and floods in west mediterranean areas: a
1224 climatic feature. Geophysical Research Abstr acts, 3.
1225
- 1226 Llasat, M. C., Llasat-Botija, M., Prat, M. A., Porcu, F., Price, C., Mugnai, A., ... & Nicolaidis, K.
1227 (2010). High-impact floods and flash floods in Mediterranean countries: the FLASH preliminary
1228 database. Advances in Geosciences, 23, 47-55.
1229
- 1230 Mason, I., 1982: A model for assessment of weather forecasts. Aust. Met. Mag., 30, 291-303.
1231
- 1232 Mass, C. F., Ovens, D., Westrick, K., & Colle, B. A. (2002). Does increasing horizontal resolution
1233 produce more skillful forecasts?: The Results of Two Years of real-Time Numerical Weather Prediction
1234 over the Pacific Northwest. Bulletin of the American Meteorological Society, 83(3), 407-430.
1235
- 1236 Mazzarella, V., Ferretti, R., Picciotti, E., & Marzano, F. S. (2021). Investigating 3D and 4D variational
1237 rapid-update-cycling assimilation of weather radar reflectivity for a heavy rain event in central Italy.
1238 Natural Hazards and Earth System Sciences, 21(9), 2849-2865.
1239
- 1240 Mittermaier, M., & Roberts, N. (2010). Intercomparison of spatial forecast verification methods:
1241 Identifying skillful spatial scales using the fractions skill score. Weather and Forecasting, 25(1), 343-
1242 354.
1243
- 1244 Nakanishi, M., & Niino, H. (2006). An improved Mellor–Yamada level-3 model: Its numerical stability
1245 and application to a regional prediction of advection fog. Boundary-Layer Meteorology, 119, 397-407.
1246
- 1247 Nakanishi, M., & Niino, H. (2009). Development of an improved turbulence closure model for the
1248 atmospheric boundary layer. Journal of the Meteorological Society of Japan. Ser. II, 87(5), 895-912.
1249
- 1250 Pakalidou, N., & Karacosta, P. (2018). Study of very long-period extreme precipitation records in
1251 Thessaloniki, Greece. *Atmospheric Research*, 208, 106-115.
1252
- 1253 Park, S. K., & Županski, D. (2003). Four-dimensional variational data assimilation for mesoscale and
1254 storm-scale applications. Meteorology and Atmospheric Physics, 82(1), 173-208.
1255
- 1256 Parrish, D., and J. Derber, 1992: The National Meteorological Center’s spectral statistical-interpolation
1257 analysis system. Mon. Wea. Rev., 120, 1747–1763, doi:10.1175/1520-
1258 0493(1992)120<1747:TNMCSS>2.0.CO;2.
1259
- 1260 Petterssen, S. (1956). Weather analysis and forecasting: motion and motion systems. McGraw-Hill.
1261
- 1262 Pichelli, E., Rotunno, R. and Ferretti, R. (2017), Effects of the Alps and Apennines on forecasts for Po
1263 Valley convection in two HyMeX cases. Q.J.R. Meteorol. Soc., 143: 2420-2435.
1264 <https://doi.org/10.1002/qj.3096>
1265



- 1266 Poterjoy, J. (2016). A localized particle filter for high-dimensional nonlinear systems. *Monthly Weather*
1267 *Review*, 144(1), 59-76.
- 1268
- 1269 Pu, Z., Li, X., Velden, C. S., Aberson, S. D., & Liu, W. T. (2008). The impact of aircraft dropsonde and
1270 satellite wind data on numerical simulations of two landfalling tropical storms during the tropical cloud
1271 systems and processes experiment. *Weather and Forecasting*, 23(1), 62-79.
- 1272
- 1273 Pytharoulis, I., Matsangouras, I. T., Tegoulis, I., Kotsopoulos, S., Karacostas, T. S., & Nastos, P. T.
1274 (2017). Numerical study of the medicane of November 2014. In *Perspectives on Atmospheric Sciences*
1275 (pp. 115-121). Springer International Publishing.
- 1276
- 1277 Pytharoulis, I. (2018). Analysis of a Mediterranean tropical-like cyclone and its sensitivity to the sea
1278 surface temperatures. *Atmospheric Research*, 208, 167-179.
- 1279
- 1280 Rabier, F., Järvinen, H., Klinker, E., Mahfouf, J. F., & Simmons, A. (2000). The ECMWF operational
1281 implementation of four-dimensional variational assimilation. I: Experimental results with simplified
1282 physics. *Quarterly Journal of the Royal Meteorological Society*, 126(564), 1143-1170.
- 1283
- 1284 Rawlins, F., Ballard, S. P., Bovis, K. J., Clayton, A. M., Li, D., Inverarity, G. W., ... & Payne, T. J.
1285 (2007). The Met Office global four-dimensional variational data assimilation scheme. *Quarterly Journal*
1286 *of the Royal Meteorological Society: A journal of the atmospheric sciences, applied meteorology and*
1287 *physical oceanography*, 133(623), 347-362.
- 1288
- 1289 Roberts, N.M. (2003) The impact of a change to the use of the convection scheme to high-resolution
1290 simulations of convective events. Met Office Forecasting Research Technical Report number: 407.
- 1291
- 1292 Roberts, N. M., & Lean, H. W. (2008). Scale-selective verification of rainfall accumulations from high-
1293 resolution forecasts of convective events. *Monthly Weather Review*, 136(1), 78-97.
- 1294
- 1295 Romero, R., Guijarro, J. A., Ramis, C., & Alonso, S. (1998). A 30-year (1964–1993) daily rainfall data
1296 base for the Spanish Mediterranean regions: First exploratory study. *International Journal of*
1297 *Climatology: A Journal of the Royal Meteorological Society*, 18(5), 541-560.
- 1298
- 1299 Romine, G. S., Schwartz, C. S., Snyder, C., Anderson, J. L., & Weisman, M. L. (2013). Model bias in
1300 a continuously cycled assimilation system and its influence on convection-permitting forecasts.
1301 *Monthly weather review*, 141(4), 1263-1284.
- 1302
- 1303 Schwartz, C. S., Kain, J. S., Weiss, S. J., Xue, M., Bright, D. R., Kong, F., ... & Wandishin, M. S.
1304 (2010). Toward improved convection-allowing ensembles: Model physics sensitivities and optimizing
1305 probabilistic guidance with small ensemble membership. *Weather and Forecasting*, 25(1), 263-280.
- 1306
- 1307 Scott, D. W. (2015). *Multivariate density estimation: theory, practice, and visualization*. John Wiley &
1308 Sons.
- 1309
- 1310 Shen, F., Song, L., Li, H., He, Z., & Xu, D. (2022). Effects of different momentum control variables in
1311 radar data assimilation on the analysis and forecast of strong convective systems under the background
1312 of northeast cold vortex. *Atmospheric Research*, 280, 106415.
- 1313



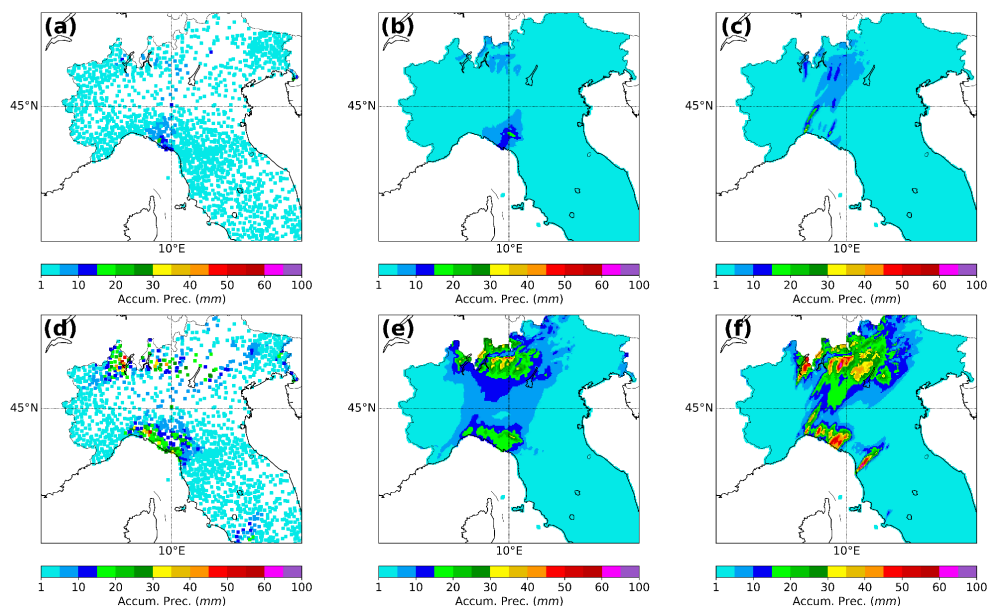
- 1314 Silverman, B. W. (2018). Density estimation for statistics and data analysis. Routledge.
1315
1316 Skamarock, W. C., Klemp, J. B., Dudhia, J., Gill, D. O., Barker, D. M., Wang, W., & Powers, J. G.
1317 (2008). A description of the advanced research WRF version 3. National Center For Atmospheric
1318 Research Boulder Co Mesoscale and Microscale Meteorology Div.
1319
1320 Stanski, H.R., L.J. Wilson, and W.R. Burrows, 1989: Survey of common verification methods in
1321 meteorology. World Weather Watch Tech. Rept. No.8, WMO/TD No.358, WMO, Geneva, 114 pp.
1322
1323 Stensrud, D. J., Bao, J. W., & Warner, T. T. (2000). Using initial condition and model physics
1324 perturbations in short-range ensemble simulations of mesoscale convective systems. Monthly Weather
1325 Review, 128(7), 2077-2107.
1326
1327 Stensrud, D. J., Xue, M., Wicker, L. J., Kelleher, K. E., Foster, M. P., Schaefer, J. T., ... & Tuell, J. P.
1328 (2009). Convective-scale warn-on-forecast system: A vision for 2020. Bulletin of the American
1329 Meteorological Society, 90(10), 1487-1500.
1330
1331 Sun, J., & Crook, N. A. (1997). Dynamical and microphysical retrieval from Doppler radar observations
1332 using a cloud model and its adjoint. Part I: Model development and simulated data experiments. Journal
1333 of the Atmospheric Sciences, 54(12), 1642-1661.
1334
1335 Swets, J. A. (1973). The Relative Operating Characteristic in Psychology: A technique for isolating
1336 effects of response bias finds wide use in the study of perception and cognition. Science, 182(4116),
1337 990-1000.
1338
1339 Tewari, M., Chen, M., Wang, F., Dudhia, W., LeMone, J., Mitchell, K., Ek, M., Gayno, G., Wegiel, J.,
1340 and Cuenca, R. H. (2004, January). Implementation and verification of the unified NOAA land surface
1341 model in the WRF model (Formerly Paper Number 17.5). In Proceedings of the 20th conference on
1342 weather analysis and forecasting/16th conference on numerical weather prediction, Seattle, WA, USA
1343 (Vol. 14).
1344
1345 Taylor, K. E. (2001). Summarizing multiple aspects of model performance in a single diagram. Journal
1346 of geophysical research: atmospheres, 106(D7), 7183-7192.
1347
1348 Tiedtke, M. I. C. H. A. E. L. (1989). A comprehensive mass flux scheme for cumulus parameterization
1349 in large-scale models. Monthly weather review, 117(8), 1779-1800.
1350
1351 Thompson, G., Field, P. R., Rasmussen, R. M., & Hall, W. D. (2008). Explicit forecasts of winter
1352 precipitation using an improved bulk microphysics scheme. Part II: Implementation of a new snow
1353 parameterization. Monthly Weather Review, 136(12), 5095-5115.
1354
1355 Torcasio, R. C., Federico, S., Comellas Prat, A., Panegrossi, G., D'Adderio, L. P., & Dietrich, S. (2021).
1356 Impact of lightning data assimilation on the short-term precipitation forecast over the Central
1357 Mediterranean Sea. Remote Sensing, 13(4), 682.
1358
1359 Tukey, J. W. (1977). Exploratory data analysis (Vol. 2, pp. 131-160).
1360



- 1361 Van Leeuwen, P. J. (2009). Particle filtering in geophysical systems. *Monthly Weather Review*,
1362 137(12), 4089-4114.
1363
1364 Velden, C., Lewis, W. E., Bresky, W., Stettner, D., Daniels, J., & Wanzong, S. (2017). Assimilation of
1365 high-resolution satellite-derived atmospheric motion vectors: Impact on HWRf forecasts of tropical
1366 cyclone track and intensity. *Monthly Weather Review*, 145(3), 1107-1125.
1367
1368 Wang, H., Huang, X. Y., Sun, J., Xu, D., Fan, S., Zhong, J., & Zhang, M. (2013, September). A
1369 comparison between the 3/4DVAR and hybrid ensemble-VAR techniques for radar data assimilation.
1370 In 35th Conference on Radar Meteorology, Breckenridge.
1371
1372 Wheatley, D. M., Stensrud, D. J., Dowell, D. C., & Yussouf, N. (2012). Application of a WRF
1373 mesoscale data assimilation system to springtime severe weather events 2007–09. *Monthly weather*
1374 *review*, 140(5), 1539-1557.
1375
1376 Whitaker, J. S., Hamill, T. M., Wei, X., Song, Y., & Toth, Z. (2008). Ensemble data assimilation with
1377 the NCEP global forecast system. *Monthly Weather Review*, 136(2), 463-482.
1378
1379
1380 Wu, X., Zhang, S., Liu, Z., Rosati, A., & Delworth, T. L. (2013). A study of impact of the geographic
1381 dependence of observing system on parameter estimation with an intermediate coupled model. *Climate*
1382 *Dynamics*, 40, 1789-1798.
1383
1384 Xiao, Q., & Sun, J. (2007). Multiple-radar data assimilation and short-range quantitative precipitation
1385 forecasting of a squall line observed during IHOP_2002. *Monthly Weather Review*, 135(10), 3381-
1386 3404.
1387
1388 Yano, J. I., Ziemiański, M. Z., Cullen, M., Termonia, P., Onvlee, J., Bengtsson, L., ... & Wyszogrodzki,
1389 A. A. (2018). Scientific challenges of convective-scale numerical weather prediction. *Bulletin of the*
1390 *American Meteorological Society*, 99(4), 699-710.
1391
1392 Yussouf, N., Dowell, D. C., Wicker, L. J., Knopfmeier, K. H., & Wheatley, D. M. (2015). Storm-scale
1393 data assimilation and ensemble forecasts for the 27 April 2011 severe weather outbreak in Alabama.
1394 *Monthly Weather Review*, 143(8), 3044-3066.
1395
1396
1397
1398
1399
1400
1401
1402
1403
1404
1405
1406
1407
1408



1409 **Appendix**



1410
1411
1412
1413
1414
1415
1416
1417
1418
1419

Fig. A1. 1-h accumulated precipitation computed from 00-01 UTC 15 October 2012 associated with (a) Observations, (b) EnKF (CNTRL) and (c) 3DVar (CNTRL). 6-h accumulated precipitation computed from 00-06 UTC 15 October 2012 associated with (d) Observations, (e) EnKF (CNTRL), (f) 3DVar (CNTRL).

Author Contribution

1420 **D. S. Carrió**: Conceptualization, Methodology, Software, Validation, Formal analysis,
1421 investigation, writing-original draft, writing-review & editing, visualization, supervision; **V.**
1422 **Mazzarella**: formal analysis, writing-review; **R. Ferretti**: formal analysis, writing-review,
1423 supervision.

1424
1425

Competing Interests

1426
1427
1428

The authors declare that they have no conflict of interest.